A Two-dimensional Magneto-optical Trap for Strontium

Eva Casotti

München 2020

Eine zweidimensionale magnetooptische Falle für Strontium

Masterarbeit an der Fakultät für Physik
Ludwig-Maximilians-Universität München

vorgelegt von

Eva Casotti

aus Trento

München, den 07. December 2020

Abstract

In this thesis, we report on a two-dimensional magneto-optical trap for strontium using permanent magnets. The purpose of this device is to produce a high-flux beam of slow atoms by collimating the atomic beam effusing from an oven. We are able to slow down the atoms and obtain a two-fold increase in the number of slow atoms. To optimize the magnetic field we constructed a three-axis translation stage for magnetic field measurements and use it to map magnetic fields in three dimensions. Based on our experimental results, we identify and discuss improvements to the effusive oven for a next-generation high-flux source of cold strontium atoms.

Contents

1 Introduction **1**

2 Laser Cooling and Trapping of Strontium **3**
2.1 Strontium . . . 3
2.2 Semi-classical Theory of Atom-light Interaction . . . 5
2.3 Atomic Beam Deceleration: the Zeeman Slower . . . 7
2.4 Atomic Beam Collimation and Trapping . . . 9
2.4.1 Optical Molasses . . . 9
2.4.2 Magneto-optical Trap . . . 12

3 Lasers **16**
3.1 Laser Theory . . . 16
3.1.1 Mechanism of Lasing . . . 16
3.1.2 Laser Diodes . . . 21
3.2 External Cavity Linear Laser . . . 24
3.3 Injection Locking . . . 28
3.3.1 Principle . . . 28
3.3.2 2D MOT Laser . . . 28

4 Oven Spectroscopy **32**
4.1 Absorption Spectroscopy . . . 32
4.1.1 Broadening Mechanisms . . . 33
4.2 Setup Description and Atomic beam model . . . 34
4.2.1 Setup . . . 34
4.2.2 Atomic Beam Model . . . 35
4.3 Measurement and Results . . . 40
4.3.1 First Region . . . 40
4.3.2 Second Region . . . 44
4.3.3 Razor Blade . . . 46

5 Magnetic Fields with Permanent Magnets **48**
5.1 Magnetic Field Measurement . . . 48
5.1.1 3-axis High Field Magnetic Measurement Stage . . . 48
5.1.2 Field Produced by a Single Magnet . . . 53
5.2 Magnetic Field Design . . . 55
5.2.1 Magnetic Field for a 2D MOT . . . 55

6 2D MOT **60**
6.1 Setup and Measurement Procedure 60
6.2 Results 63

7 Conclusion and Outlook **67**

References **69**

Acknowledgements **75**

A Our Strontium Oven **77**
A.1 Current Design 77

B Zeeman Slower Repumping **82**
B.1 Laser Characterization 83
B.2 Atom Number Measurement 85

List of Tables

2.1 Strontium Isotopes 3

5.1 Stepper Motors Specifications 51

6.1 Slow Atom Number Comparison 65

B.1 Laser Diode Specifications 82

List of Figures

2.1 Strontium Level Scheme . . . 4
2.2 Scattering Rate Saturation . . . 7
2.3 Zeeman Slower . . . 9
2.4 Optical Molasses Force Profile . . . 10
2.5 MOT Working Principle . . . 13

3.1 Laser Level Schemes . . . 19
3.2 P-n Junction Scheme . . . 22
3.3 Heterostructure Scheme . . . 23
3.4 ECDL Render . . . 25
3.5 Laser Protection Board Diagram . . . 27
3.6 Injection Lock Laser Optics Setup . . . 28
3.7 Power vs Current of the 500 mW Laser . . . 30
3.8 500 mW Laser Spectrum . . . 30

4.1 Absorption and Fluorescence . . . 32
4.2 Vacuum Chamber . . . 35
4.3 Knudsen Number as a Function of Temperature . . . 37
4.4 Angular Distribution in Molecular Flow Regime . . . 38
4.5 Comparison between the Molecular Flow Regime and the Intermediate Regime . . . 39
4.6 Absorption Spectra for the First Spectroscopy Region . . . 41
4.7 Fit of Absorption Spectra . . . 41
4.8 Viewports Baking . . . 42
4.9 First Region Spectra after Pumping . . . 43
4.10 Second Spectroscopy Region Spectra . . . 44
4.11 Second Spectroscopy Region Multipass Setup . . . 45
4.12 Absorption Spectra for the Second Spectroscopy Region: Multipass Case 45
4.13 Razor Blade Spectra . . . 46

5.1 Stepper Motor Cross Sections . . . 50
5.2 Three-axis Translation Stage . . . 52
5.3 Magnetic Field of a Permanent Magnet . . . 53
5.4 Single Magnet Magnetic Field Fit . . . 53
5.5 Magnets arrangement . . . 55
5.6 Field along the z-axis . . . 56
5.7 Quadrupole Field xy Plane . . . 56
5.8 Quadrupole Field xz Plane . . . 57

5.9 Permanent Magnets Mount 58
5.10 Magnetic Field Measurement 59

6.1 2D MOT Arm Optics 60
6.2 Laser Table 61
6.3 Double Pass AOM 62
6.4 Main Experiment Blue Laser System 63
6.5 1D Molasses Cooling as a Function of Temperature 64
6.6 1D Molasses Cooling as a Function of Power 64
6.7 1D Molasses Cooling as a Function of Razor Blade Position 65
6.8 Attempt of Deflection of the Atomic Beam 66

A.1 Oven Exploded View 77
A.2 Crucible and Nozzle Render 78
A.3 Heating Circuit Setup 79
A.4 Oven Temperatures 80

B.1 Zeeman Repump Laser Mount 82
B.2 Zeeman Repump Laser Diodes Power vs Current 83
B.3 Zeeman Repump Laser Spectra 84
B.4 Zeeman Repump Laser Spectrum Filtered 84

Chapter 1

Introduction

Ultracold quantum gases in optical lattices have been demonstrated to constitute a toolbox to study a lot of different phenomena. They have been employed for the simulation of strongly correlated systems [1, 2], allowed studying of topological phases [3], Rydberg physics [4], dipolar quantum gases [5], and optical clocks [6]. This is possible thanks to the high control over parameters such as interaction strength, potential depth, spin and system size. The construction of quantum gas microscopes has enabled single site resolution and addressing, opening a new window on the physics of ultracold atoms in optical lattice [7–9].

Alkali atoms have been the first elements to be used in these experiments due to the presence of favorable cooling transitions, but the interest in alkaline earth atoms has grown in the recent years. These atoms have a richer level structure, which includes transitions that allow producing high-quality state-dependent lattices [10, 11]. In our experiment we aim to build a strontium quantum gas microscope for quantum simulations with state-dependent lattices. Strontium offers a variety of transitions with linewidths ranging from the megahertz to the millihertz regime. The doubly forbidden $^1S_0 \rightarrow ^3P_0$ transition, with a linewidth of about 1 mHz and a wavelength of 698 nm, is now a frequency standard [12]. The transition arises in the fermionic isotope, ^{87}Sr, which possesses nuclear spin $\frac{9}{2}$. This non-zero nuclear spin has led to proposals for the study of systems with SU(N) symmetry, which means that collisions cannot distinguish between the nuclear spin states because only the electron clouds collide. Having 10 different spin states ^{87}Sr is a good candidate for simulation of exotic quantum phases [13].

No matter what system we are studying, every experiment is limited by the cycle time. In clocks, readout time leads to degradation of the clock stability [12]. Quantum simulation experiments require a lot of averaging, and thus also need a high repetition rate [14]. A larger number of repetitions N would improve the averaging result in a dramatic way since the error scales as $1/\sqrt{N}$. For this reason, we want the highest number of atoms in the fastest time scale possible. A first step in this direction would be a faster loading rate of the magneto-optical traps used to cool the atoms. With this purpose in mind, oven based on microchannels arrays have been used in many experiments [15, 16]. The microchannels collimate the atomic beam at the moment of effusion from the nozzle. Still, these ovens tend to clog and exhibit a quite broad transverse velocity distribution. Common techniques used to decelerate the atoms act on the longitudinal ve-

locity distribution and leave the orthogonal distribution unchanged. One possible way of enhancing the flux by collimating the atomic beam is a two-dimensional magneto-optical trap (2D MOT). The feasibility of this setup, which traps and cools atoms in two directions leaving the third unchanged, has already been demonstrated for strontium [17, 18]. 2D MOTs have been implemented for rubidium [19, 20], potassium [21], cesium [22–24], sodium [25, 26], and lithium [27].

The aim of this thesis is to build a two-dimensional magneto-optical trap for our experiment. This is part of bigger project with the aim of increasing the efficiency of our atomic source. We would like to build a 2D MOT with permanent magnets, which are less expensive and require less engineering than electromagnets. The 2D MOT could help us to obtain a high-flux beam of slow atoms and allow separating the cooled atoms from the thermal atoms, and blocking any line of sight between the oven output and the following steps of our sequence. Other experiments achieve this purpose with the aid of a push beam that allows also to tune the atomic beam velocity. We would like to do it by tilting the magnetic field direction.

In Chapter 2 we discuss the most important properties of strontium and review the theory of atom-light interaction focusing on setups for laser cooling and trapping of neutral atoms. We then describe the basic tools for every experiment with ultracold quantum gases: lasers. In Chapter 3 we briefly introduce the basics of the lasing mechanism and describe the two setups that we will use in this thesis. Then we need to understand the source of the atomic beam that we will use, namely the first generation of our new strontium oven. With this purpose in mind, in Chapter 4 we discuss absorption spectroscopy and use it to measure the parameters of the atomic beam. To design the magnetic field for the 2D MOT, we describe a three-axis translation stage for high magnetic field measurement, in Chapter 5. Finally we use absorption spectroscopy to measure the effect of our two-dimensional magneto-optical trap on the atomic beam in Chapter 6.

Chapter 2

Laser Cooling and Trapping of Strontium

The two-dimensional magneto-optical trap fundamentally relies on *radiation pressure*, which is a non-conservative force resulting from the interaction of atoms with light. In this chapter, we introduce this interaction and learn how to use light to cool and trap atoms and, in particular, strontium. The theoretical discussion is mainly based on Ref. [28].

2.1 Strontium

Before discussing light-matter interaction and how we can cool and trap atoms, we will introduce the atomic species we will be working with: strontium. This will allow addressing concrete examples in the next sections.

Strontium naturally has four isotopes, which are recorded in Table 2.1. Three out of four are bosons and have no nuclear spin, while ^{87}Sr is a fermion and has a nuclear spin of $\frac{9}{2}$.

Isotope	Abundance	Nuclear Spin	Statistics
^{84}Sr	0.56%	0	Bosonic
^{86}Sr	9.86%	0	Bosonic
^{87}Sr	7.00%	$\frac{9}{2}$	Fermionic
^{88}Sr	82.58%	0	Bosonic

Table 2.1 Strontium isotopes and their basic features.

Strontium is an alkaline-earth atom, and has two valence electrons, which produce a complex electronic structure made of singlet and triplet states similar to helium. As shown in Fig. 2.1, strontium offers various transitions with different linewidths, from strongly allowed transitions in the megahertz regime to intercombination transitions connecting singlet and triplet states in the kilo and millihertz regime.

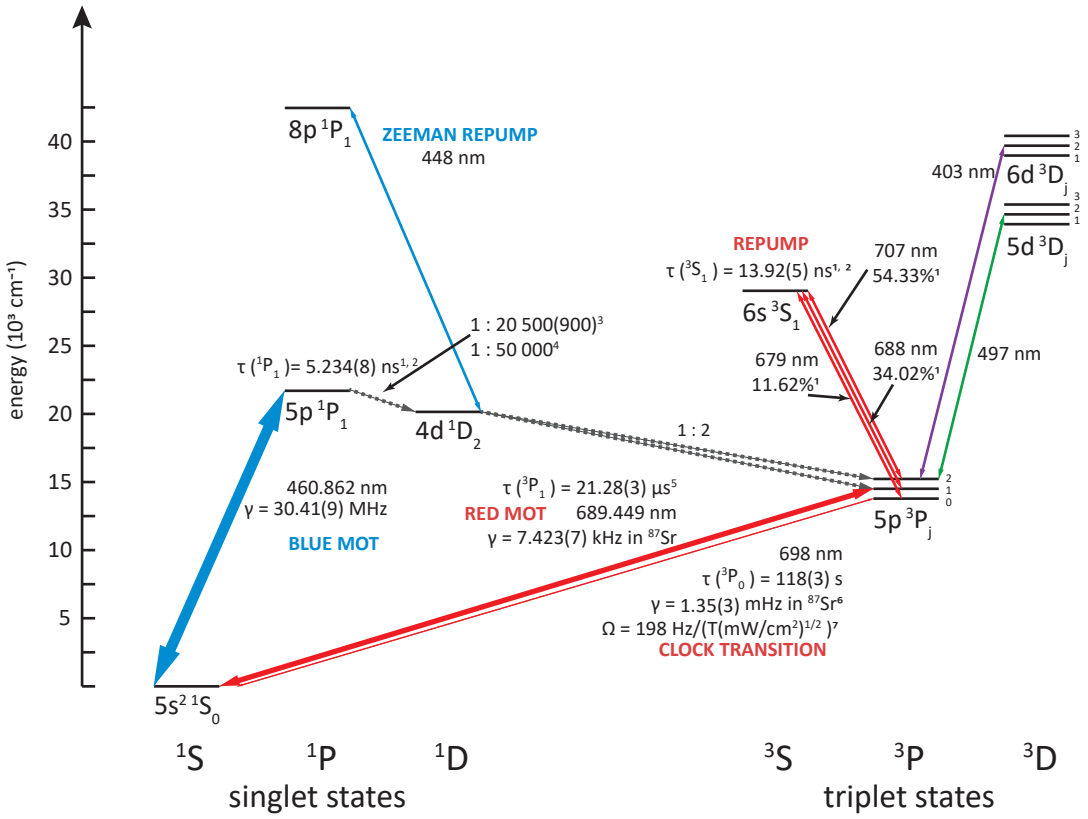

Figure 2.1 Relevant strontium level structure. Spectroscopic data is taken from Refs. [1][29] [2][30] [3][31] [4][32] [5][33] [6][34] [7][35].

There are two transitions used for cooling, the blue one at 460.86 nm, and the red one at 689.45 nm. We will postpone the discussion on why and how these transitions are used to the next sections.

Another important feature is the existence of metastable states. The triplet states ^{3}P are metastable: in theory, an atom in these states cannot decay into the ground state $^1S_0$ because of dipole selection rules. These states still decay, because LS-coupling is violated [36], but the states are still long-lived, especially $^3P_2$, which has a lifetime of several minutes [37, 38]. The lowest triplet state $^3P_0$ is also long-lived, and the transition $^1S_0 \rightarrow ^3P_0$ is doubly forbidden since transitions between levels with $J = 0$ are not allowed. However, in the case of fermionic strontium, the non-zero nuclear spin allows hyperfine interactions, which mix this state with $^3P_1$, $^3P_2$ and $^1P_1$ producing the *clock transition* $^1S_0 \rightarrow ^3P_0$ at 698 nm [39]. It has a lifetime of about 120 s and is used as a frequency standard in optical clocks [12].

The presence of metastable levels complicates the cooling process and requires addi-

tional transitions to make laser cooling efficient and to avoid losing atoms. We call these transitions *repump transitions* since they are used to pump the atoms back into a state from which they can reach the ground state. In Fig. 2.1 we highlighted some of them. We will explain the different schemes in Section 2.4.2. Let us now introduce light-matter interaction and focus on one of the resulting forces: the scattering force.

2.2 Semi-classical Theory of Atom-light Interaction

The starting point for understanding atom-light interaction is the two-level system. Let us approximate an atom as a point-like system characterized by an excited state $|e\rangle$ and a ground state $|g\rangle$. The energy difference between the two levels is $E = \hbar\omega_{eg}$, while the spontaneous emission rate is $\Gamma = 1/\tau$, with τ the natural lifetime. The other element that we need is the laser light, which is treated as a classical field in the plane-wave approximation:

$$\mathbf{E}(\mathbf{r}, \mathbf{t}) = E_0 \mathbf{e} \cos(\omega_L t - \mathbf{k}_L \cdot \mathbf{r}), \tag{2.1}$$

with $\mathbf{e}$, $\omega_L = 2\pi c/\lambda_L$, and $\mathbf{k}_L$ being the polarization vector, the light frequency, and the wave vector, respectively. Approximating the atom as a two-level system may seem too strong since atoms have a complex multilevel structure, as we have seen for strontium in Section 2.1. However, if light couples just two levels near resonantly, it can describe the real case very well. Nevertheless, if atoms decay from the excited level to a third one, optical pumping is required to close the transition and go back to the simple two-level picture. In a few words, optical pumping exploits light to transfer atoms to higher energy levels. If the laser's frequency matches the energy level separation, the atom gets excited. This simple mechanism is exploited in some types of lasers and in atomic physics to select particular state configurations or improve cooling efficiency. We will see how we apply this method in Section 2.4.2.

We will work with the system's Hamiltonian in the dipole approximation, which neglects spatial variations of the electromagnetic field on the atomic scale:

$$H = \hbar\omega_{eg}|e\rangle\langle e| - \mathbf{d} \cdot \mathbf{E}, \tag{2.2}$$

where $\mathbf{d} = d_{eg}(|g\rangle\langle e| + |e\rangle\langle g|)$ is the dipole operator and $\mathbf{E}$ is the electric field written in Eq. (2.1). The coupling between the atom and the field is described using the Rabi frequency, defined as:

$$\Omega \equiv -\mathbf{d} \cdot \mathbf{E}/\hbar. \tag{2.3}$$

The problem can be rewritten in terms of the density matrix, which allows taking spontaneous emission into account. By doing this, one gets four equations for the level pop-

ulations ρ_{gg} and ρ_{ee}, and the coherences ρ_{ge} and ρ_{eg}, called the *Optical Bloch Equations*[1]:

$$\begin{aligned}
\frac{d\rho_{gg}}{dt} &= +\Gamma\rho_{ee} + \frac{i}{2}(\Omega^*\tilde{\rho}_{eg} - \Omega\tilde{\rho}_{ge}) \\
\frac{d\tilde{\rho}_{ge}}{dt} &= -\left(\frac{\Gamma}{2} + i\Delta\right)\tilde{\rho}_{ge} + \frac{i}{2}\Omega^*(\rho_{ee} - \rho_{gg}) \\
\frac{d\tilde{\rho}_{eg}}{dt} &= -\left(\frac{\Gamma}{2} - i\Delta\right)\tilde{\rho}_{ge} + \frac{i}{2}\Omega(\rho_{gg} - \rho_{ee}) \\
\frac{d\rho_{ee}}{dt} &= -\Gamma\rho_{ee} + \frac{i}{2}(-\Omega^*\tilde{\rho}_{eg} - \Omega\tilde{\rho}_{ge}),
\end{aligned} \tag{2.4}$$

where $\Delta = \omega_L - \omega eg$ is the detuning, $\tilde{\rho}_{ij} = \rho_{ij}e^{-i\Delta t}$, and the * denotes the complex conjugate. Here, the decay is assumed to be described by just the natural lifetime.

What we are interested in is the steady-state solution of these equations, obtained by setting the time derivative to zero. The steady-state excited state population is then

$$\rho_{ee}^{ss} = \frac{s_0/2}{1 + s_0 + (2\Delta/\Gamma)^2}, \tag{2.5}$$

with the *on-resonance saturation parameter* s_0, which is given by the *saturation intensity* $I_s \equiv \pi hc/3\lambda^3\tau$:

$$s_0 \equiv 2|\Omega|^2/\Gamma^2 = \frac{I}{I_s}. \tag{2.6}$$

This result implies, for the scattering rate Γ_{sc}, that

$$\Gamma_{\mathrm{sc}} = \Gamma\rho_{ee}^{ss} = \frac{s_0\Gamma/2}{1 + s_0 + (2\Delta/\Gamma)^2}. \tag{2.7}$$

From this rate, it is pretty straightforward to obtain the scattering force expression. Every time the atom absorbs a photon, there is a momentum transfer from the light field to the atom given by the photon momentum $\hbar\mathbf{k}$. The atom can then spontaneously emit a photon. Spontaneous emission happens in a random direction, thus its effect on the atomic momentum averages out after a few cycles. This means that the result of absorption followed by spontaneous emission is a net force along the laser light direction:

$$\mathbf{F}_{\mathrm{sc}} = \hbar\mathbf{k}\Gamma\rho_{ee}^{ss} = \frac{\hbar k s_0\Gamma/2}{1 + s_0 + (2\Delta/\Gamma)^2}. \tag{2.8}$$

The equation displays the momentum change given the emission rate and the probability of being in the excited state. This is the so-called *radiation pressure*, describing the pressure exerted on atoms during the scattering process.

[1] To solve the problem analytically, we make use of another approximation: the *rotating wave approximation*, which neglects fast oscillating terms. Further details can be found in Ref. [28]

2.3 Atomic Beam Deceleration: the Zeeman Slower

Let us now take an atomic beam into account. An atomic beam is a collimated flux of neutral atoms. In our case, it is produced by an atomic oven, where strontium is heated up and then effuses through a nozzle of microcapillaries, which collimate the beam. More on how our beam is produced and on its characterization can be found in Chapter 4.

Now that we know the scattering force expression, it is easy to understand that one could use a laser beam to slow down an atomic beam. As we said, the net force is directed along the laser beam direction; suppose we now take light propagating in the opposite direction to the atoms: the result is a deceleration of the atoms. But which atoms can we actually affect? What we have seen in Section 2.2 is valid for an atom at rest. For an atom moving with velocity $\mathbf{v}$ the detuning changes due to the Doppler shift:

$$\Delta' = \Delta - \mathbf{k} \cdot \mathbf{v}. \tag{2.9}$$

Let us have a look at the scattering rate taking the Doppler effect into account. As shown in Fig. 2.2, the scattering rate saturates for high intensities due to the factor s_0 in the denominator. The maximum force obtainable is, according to Eq. (2.8), $\mathbf{F}_{\max} = \hbar \mathbf{k} \Gamma/2$. At the same time, higher intensities produce a broadening of the peak, so higher-velocity atoms are addressed.

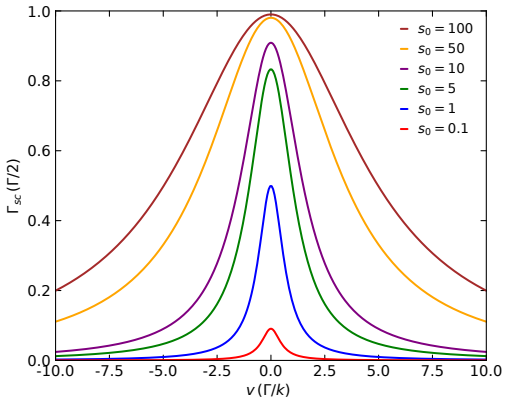

Figure 2.2 Scattering rate profile as a function of the saturation parameter s_0. The maximum saturates for high values of s_0 while the peak gets broader. This means that for high intensities, more atoms are affected. The scattering rate is given as a fraction of the maximum $\Gamma/2$, and the laser light is assumed to be resonant.

To maximize the force and thus to efficiently slow down the beam, we need to be on resonance. For this reason, we need to compensate for the Doppler shift reduction as the atoms slow down. This can be done by actively sweeping the laser beam's frequency

[40–42], or by exploiting the Zeeman effect with a *Zeeman slower* [43, 44]. In the second case, a spatially varying magnetic field is used to tune the atomic level separation. In this way, atoms can be kept in resonance. In the presence of a magnetic field, atoms experience an energy shift given by:

$$\Delta E = -\boldsymbol{\mu} \cdot \mathbf{B} = g_J m_J \mu_B B(\boldsymbol{r}), \tag{2.10}$$

where $\boldsymbol{\mu} = -g_J \mu_B \boldsymbol{J}$ is the magnetic moment, $\boldsymbol{J}$ is the total angular momentum, g_J the Landé factor, and m_J is the angular momentum projection along the quantization axis defined by the magnetic field. This shift causes an additional contribution to the detuning:

$$\Delta' = \Delta - \mathbf{k} \cdot \mathbf{v} + \frac{g_J m_J \mu_B}{\hbar} B(\boldsymbol{r}). \tag{2.11}$$

Let us look at the one-dimensional problem. We want to find the form of the magnetic field that we need to apply to uniformly decelerate an atom having initial velocity v_0 along the z-axis. To efficiently slow down the atom, we need to be on resonance. If we take $\Delta = 0$ and set Δ' to zero we get a condition for $B(z)$. In this case, an atom with mass M experiences a constant deceleration $a = \hbar k \Gamma / 2M$. We find

$$B(z) = \frac{\hbar k v(z)}{g_J m_J \mu_B} = \frac{\hbar k}{g_J m_J \mu_B} \sqrt{v_0^2 - 2az} = B_0 \sqrt{1 - z/z_0}, \tag{2.12}$$

where $z_0 \equiv M v_0^2 / \hbar k \Gamma$ the length of the non-zero field region and $B_0 \equiv \hbar k v_0 / g_J m_J \mu_B$. Such a field is usually obtained with a solenoid having layers of decreasing length, as shown in Fig. 2.3. Further details on how we could improve the performance of our Zeeman slowers can be found in Appendix B.

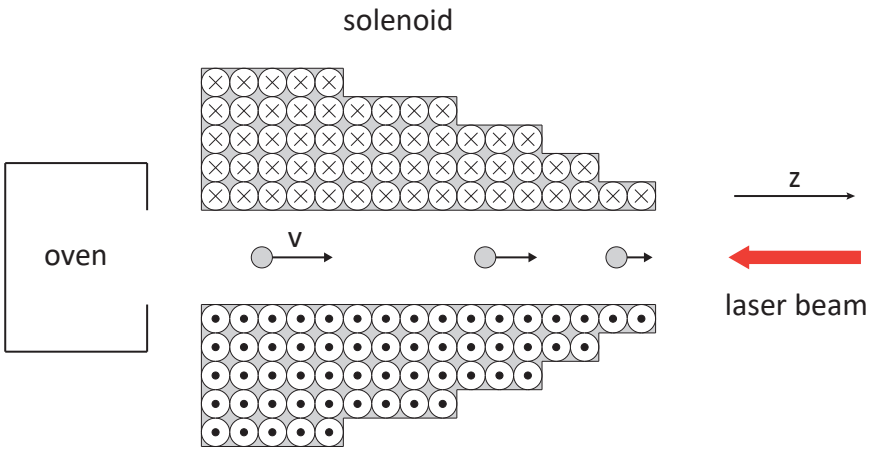

Figure 2.3 Scheme of a Zeeman slower obtained via a solenoid with a varying number of windings along z. Figure adapted from Ref. [45].

2.4 Atomic Beam Collimation and Trapping

2.4.1 Optical Molasses

So far, we have just looked at the effect of a single laser beam. We want to see now what happens if we apply more beams. We will treat this case assuming that the light intensity is low enough to avoid "coupling" between different beams[2]. In this case, the action of the different beams can simply be added. If we take two counterpropagating beams, the total force is:

$$\mathbf{F}_{\mathrm{sc}} = \frac{\hbar \mathbf{k} \Gamma}{2} \left(\frac{s_0}{1 + s_0 + [2(\Delta - kv)/\Gamma]^2} - \frac{s_0}{1 + s_0 + [2(\Delta + kv)/\Gamma]^2} \right). \tag{2.13}$$

For small velocities, we can approximate Eq. (2.13) as

$$\mathbf{F}_{\mathrm{sc}} \sim \frac{8\hbar k^2 \Delta s_0 \mathbf{v}}{\Gamma(1 + s_0 + (2\Delta/\Gamma)^2)^2} \equiv -\beta \mathbf{v}. \tag{2.14}$$

[2] If they were coupled, we should, for example, take into account that an atom excited by one beam could emit stimulated by another.

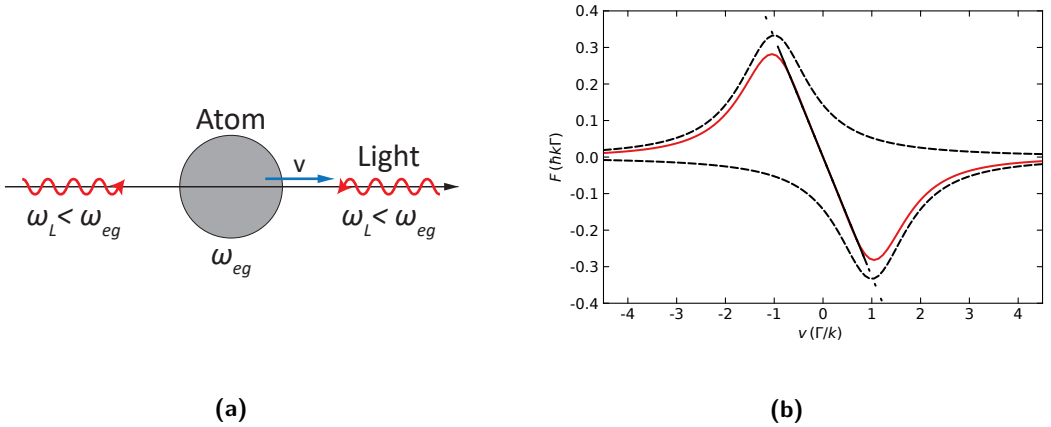

(a) **(b)**

Figure 2.4 (a) Optical molasses principle. Red detuned light is propagating in the opposite direction of an atom, which will see this light shifted towards resonance. The atom will thus experience a frictive force. (b) Optical molasses force profile. The solid red line shows the total force that acts on the atom in the case of two "independent" laser beams. The dashed black curves show the forces due to the two single laser beams, while the straight line underlines that for small velocities, the force resembles a friction force.

As displayed in Fig. 2.4 and Eq. (2.14), for small velocities and negative detuning (*red-detuned* light) the force looks like a friction force with damping coefficient β. For this reason, this configuration is called *optical molasses*. An atom moving in a given direction will see the counterpropagating light shifted towards resonance and will consequently be affected more by this beam than by the other one. This produces a deceleration. The reduction in kinetic energy corresponds to a decrease in temperature thanks to the equipartition theorem[3].

Limitations

The first limit of molasses cooling is the temperature that can be reached. Of course, it is not possible to cool the atoms to zero temperature because two opposite mechanisms compete. The first one is the cooling process due to the friction force; the second is the heating induced by the scattering of light into random directions. The temperature that can be reached is the one at which the balance between cooling and heating occurs. This happens at the *Doppler temperature*, with its minimum value

$$T_D = \frac{\hbar\Gamma}{2k_B}, \tag{2.15}$$

[3] Although the system is not in thermodynamic equilibrium, the atomic velocity distribution can still be described by a Maxwell-Boltzmann distribution. Therefore we can define an effective temperature using the average square velocity $\langle v^2 \rangle$: $\frac{1}{2}k_B T = \frac{1}{2}m\langle v^2 \rangle$, with m the mass of the atom.

when $\Gamma = \Delta/2$. This temperature is actually not the lowest achievable. Other cooling mechanisms can bring the atoms towards another limit, the *recoil temperature*[4]

$$T_{RC} = \frac{\hbar^2 k_L^2}{2mk_B}. \tag{2.16}$$

An easy way to understand this limit is the following: let us assume that we have been able to stop the atom with the previous absorption event. The atom is now excited and will, at some point, spontaneously emit a photon. The recoil of this last photon will transfer energy to the atom. This energy can then be converted to temperature to get the expression in Eq. (2.16).

Let us now have a look at the specific case of strontium. We already mentioned the two cooling transitions. The blue transition, $^1\mathrm{S}_0 \rightarrow ^1\mathrm{P}_1$, has a wavelength of 460.86 nm and a natural linewidth of $2\pi \times 30.41(9)$ MHz, which is useful for initial cooling of the atoms. It is usually employed in Zeeman slowers and magneto-optical traps; we will learn about the trap in Section 2.4.2. We will exploit this transition also to do some simple absorption spectroscopy. This transition produces the highest radiation pressure due to its large linewidth. At the same time, it has a relatively large Doppler temperature:

$$T_D^{\mathrm{blue}} = 0.7 \text{ mK}. \tag{2.17}$$

To cool further, we need the $^1\mathrm{S}_0 \rightarrow ^3\mathrm{P}_1$ red transition at 689.45 nm with a $2\pi \times 7.423(7)$ kHz linewidth, which is allowed due to mixing with the $^1\mathrm{P}_1$ state [39]. This transition allows cooling close to the recoil limit

$$T_{RC}^{\mathrm{red}} = 230 \text{ nK}. \tag{2.18}$$

The Doppler temperature is here even lower:

$$T_D^{\mathrm{red}} = 180 \text{ nK}. \tag{2.19}$$

The drawback of this transition is that the narrow linewidth makes the cooling less efficient because the scattering force is reduced.

Another limitation of optical molasses is that we cannot trap the atoms just with the radiation pressure. This is a consequence of the *optical Earnshaw theorem*, which states that a small dielectric particle cannot be trapped by using only the scattering force of optical radiation pressure [46]. For this purpose, we can build a magnetic trap, a dipole trap, or combine optical molasses and magnetic fields to obtain a magneto-optical trap depending on the atomic species that we are using and what we want to achieve. We

[4] These mechanisms are based on the fact that the two-level system approximation breaks down. Zeeman shifts and polarization gradients are responsible for sub-Doppler mechanisms. There are several schemes; one is *Sisyphus cooling* which is obtained via two counterpropagating molasses beams having opposite linear polarization.

will briefly mention the first two options and then move to the third one, which is the focus of this thesis.

Magnetic Trap

If we want to trap our atoms, a possibility is offered by inhomogeneous magnetic fields. In the presence of a magnetic field, atoms experience an energy shift given by Eq. (2.10), which is valid for a spatially varying field if the atoms are slow enough that m_J is constant. This happens if the variation of the field orientation takes place on a timescale slower than the Larmor precession frequency $\omega_L = g_J eB/2m_e$ so that the dipole can follow the change in magnetic field adiabatically. Here e is the electron charge and m_e the electron mass.

If the magnetic moment is aligned with the field, the atom will be attracted to a higher field region (*high-field-seeking* atoms) while, if it is opposite to the field, the atom will be attracted to lower field regions (*low-field-seeking*). It is impossible to produce a local field maximum, but we can produce a local minimum to trap low-field seeking atoms. This is the first drawback of this kind of trap: the atoms need to have non-zero angular momentum, and not every m_J can be trapped. For this reason, magnetic traps work for alkali atom ground states but not for alkaline-earth atom ground states.

Magnetic traps can be obtained with many different configurations; the simplest one is a quadrupole trap produced by two aligned coils with opposite current.

Dipole Trap

Another way to trap atoms is by using the *dipole force*. This force is the other component, additional to the radiation pressure, that results after a full treatment of the light-atom interaction. It has the following expression and depends on the spatial gradient of the light intensity:

$$\boldsymbol{F}_{\mathrm{d}} \simeq -\frac{\hbar\Gamma^2}{8\Delta I_s}\boldsymbol{\nabla} I(r). \tag{2.20}$$

As seen in Section 2.3, the radiation pressure is a dissipative force, on the other hand, the dipole force is conservative. This force produces a potential that has its minimum (maximum) where the intensity is maximal (minimal) for red-detuned (blue-detuned) light. This kind of trap can be used to trap alkaline-earth atoms. The trapping forces generated optical dipole traps are relatively weak; thus, a cooling step is fundamental before loading into the trap. We will now move to the magneto-optical trap, the focus of this thesis.

2.4.2 Magneto-optical Trap

Let us now consider again the 1D molasses setup shown in Fig. 2.4 (b), this time adding a magnetic field $B(z) = -bz$. The axis z is the one along which light is propagating, and

b is the magnetic field gradient. This field can be produced, for example, using two anti-Helmholtz coils, as shown in Fig. 2.5 (a). Let us look at the effect of the field on the atomic levels. For simplicity, we will take an atom whose ground state has total angular momentum $J_g = 0$ while the excited state has $J_e = 1$, which is also the configuration of low energy states in alkaline-earth atoms like strontium as explained in Section 2.1. The ground state is not affected by the field presence. On the other hand, the excited state gets split into three Zeeman sublevels with a spatially dependent shift:

$$\Delta E = \mu_B g_{J_e} m_{J_e} b z, \tag{2.21}$$

with the Bohr magneton μ_B, the Landé g-factor g_{J_e}, and the angular momentum projection of the excited state along the quantization axis m_{J_e}. Circularly polarized laser beams will produce a spatially dependent force that will push the atoms towards zero. As shown in Fig. 2.5 (b) red-detuned σ^+ light coming from the left will address $m_{J_e} = +1$ atoms while σ^- will act on $m_{J_e} = -1$. The result is a force that pushes the atoms towards the center.

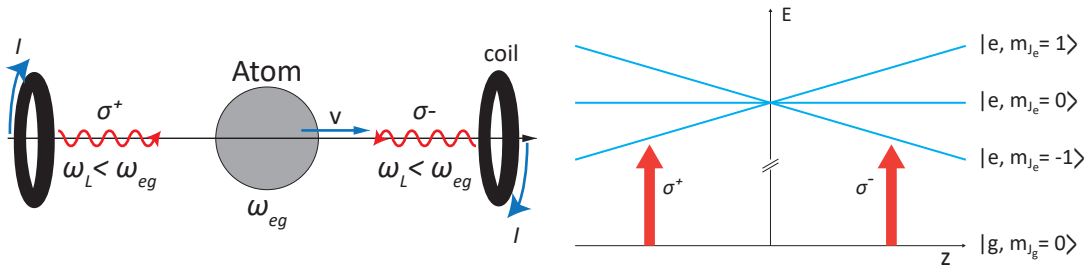

(a) **(b)**

Figure 2.5 (a) Schematic of the magneto-optical trap principle in 1D. (b) Level splitting due to the Zeeman effect. The figures have been adapted from Ref. [45].

Such a spatial dependent force has the following expression:

$$\begin{aligned}\mathbf{F}_{\text{sc}} = &\frac{\hbar \mathbf{k} \Gamma}{2} \Bigg(\frac{s_0}{1 + s_0 + [2(\Delta - kv - \mu_B g_J m_J b z/h)/\Gamma]^2} \\ &- \frac{s_0}{1 + s_0 + [2(\Delta + kv + \mu_B g_J m_J b z/h)/\Gamma]^2} \Bigg).\end{aligned} \tag{2.22}$$

For small velocity and displacement, the force can be approximated by:

$$F_{\text{sc}} \equiv -\beta \mathbf{v} - \kappa \mathbf{z}, \qquad \kappa = \frac{g_{J_e} \mu_B b}{\hbar k_L} \beta. \tag{2.23}$$

The force in Eq. (2.23) describes a damped harmonic oscillator. The component given by the magnetic field is conservative, thus the achievable temperature is still determined by molasses parameters. What we did so far was one-dimensional, but one can easily extend to the two- and three-dimensional case.

Magneto-optical Trap for Strontium

Blue and Red MOTs We already mentioned several times the blue and red cooling transitions. We said that with the red one, we could achieve lower temperatures, but the efficiency is also lower, and it is thus impossible to trap a thermal beam directly. For this reason, the so-called blue MOT is used first to subsequently load the red MOT.

A fundamental limit to the trap efficiency is set by the *capture velocity*, atoms traveling faster than this cannot be trapped. In the blue MOT case, the capture velocity is ~ 30 m/s [47], while the typical velocity of atoms effusing from the oven at the operating temperature is around 400 m/s. This means we will lose most of the atoms unless we slow them down before they get to the MOT region. Moreover, we need to avoid collisions between trapped atoms and hot background gas since the momentum change would kick the atoms out of the trap. These simple arguments underline the necessity of a high-flux source of slow atoms. To overcome these issues, we can build Zeeman slowers and two-dimensional magneto-optical traps (2D MOTs).

The red MOT has a capture velocity $v_c = \Gamma/2k$ on the order of the mm/s, but the effect of the blue MOT stage is already enough to load most of the atoms. In the main experiment, we still artificially increase the capture velocity by scanning the red laser from far red-detuned to across the resonance. Further information on this method and how it is implemented can be found in Ref. [29].

Repump schemes Another cause of inefficiency is a consequence of the level structure. We mentioned the existence of metastable states in Section 2.1. If during the cooling process our atoms decay in one of these, they are lost. During the blue MOT step, atoms can decay on the $^1\mathrm{P}_1 \rightarrow {}^1\mathrm{D}_2$ transition. This decay is non-negligible, happening with a ratio of 1:50 000. From this state, atoms can then decay into the triplet state $^3\mathrm{P}_2$. We need optical pumping to pump them back to a level where we can cool them. There are several possibilities to close the $^1\mathrm{S}_0 \rightarrow {}^1\mathrm{P}_1$ transition.

In the main experiment [29], a 707 nm laser is used to optically pump atoms from $^3\mathrm{P}_2$ to $^3\mathrm{S}_1$ from which they can decay again into any $^3\mathrm{P}_J$. If they decay again into $^3\mathrm{P}_2$, they will get pumped back. If they decay into $^3\mathrm{P}_0$ instead, a 679 nm laser pumps them back to $^3\mathrm{S}_1$. At some point, they will all reach $^3\mathrm{P}_1$, and from this decay to $^1\mathrm{S}_0$.

Another popular scheme requires pumping back to 5s5d $^3D_2$ with a 497 nm laser or to 5s6d $^3D_2$ with a 403 nm one. One laser is enough since the decay into $^3P_0$ is a higher-order process.

Another possibility, which we would like to implement for our Zeeman slower, is intercepting the atoms before they decay into the triplet state. For this we want to pump from 5s4d $^1D_2$ to 5s8p $^1P_1$ via a 448 nm laser. Further details will be explained in Appendix B.

Let us now introduce the concept of a two-dimensional magneto-optical trap, which could help us to produce a high-flux beam of slow atoms to increase the efficiency of the whole cooling process.

Two Dimensional Magneto-optical Trap

A two-dimensional magneto-optical trap acts in the plane given by four light beams and leaves the orthogonal direction of the atomic velocity unperturbed. As in the 1D case, we have the cooling effect of optical molasses and the trapping one of the magnetic field, which has the following expression:

$$\mathbf{B} = b\mathbf{x} - b\mathbf{y}, \tag{2.24}$$

where the light beams are on the xy-plane, and the atomic beam is propagating along the z-axis. Such a field can be produced, for example, by two pairs of coils in Anti-Helmholtz configuration or via permanent magnets. The result is a magnetic field gradient along the light beam directions and a zero-field line along the z-axis.

With this two-dimensional trap, we should obtain a cigar-shaped cloud of enhanced brightness compared to the original atomic beam. Besides, since the atoms are driven to the zero-field axis, changing its direction could allow the decoupling of the slow atomic beam from the thermal part. For these reasons, the 2D MOT is a good tool to improve an atomic source's efficiency. We will go into the details of this system in Chapter 6.

In this chapter, we discussed the cooling and trapping of strontium, and we have understood how important it is to build a high-flux source of slow atoms. With this purpose in mind, we will build a 2D MOT. But before moving to this setup, we need to understand the tools we are going to use and how we will measure and characterize the effect of this 2D MOT. For this reason, we will now talk about the lasers we will use.

Chapter 3

Lasers

In the previous chapter, we have dealt with atom-light interaction basics and some common setups used in experiments with ultracold quantum gases to cool and trap atoms. Before moving to the main topic of this thesis, namely the realization of a 2D MOT, we need a tool to measure the atom number and quantify the improvement over the current source produced by the 2D MOT. Here, we review the mechanism of lasing and describe our setups. In the first Section 3.1 of this chapter, we will repeat some laser theory basics following the discussion in Ref. [48]. Moreover, we will get an overview of laser diodes (LDs) and their features, focusing on blue ones; this Section will be based on Ref. [49]. In the following Section 3.2, we will briefly look at a particular setup: the *external cavity linear laser*, which we will exploit to characterize the atomic beam. In the third Section 3.3, we will review the mechanism of injection locking. This will allow the construction of the laser setup required to build our magneto-optical trap.

3.1 Laser Theory

3.1.1 Mechanism of Lasing

The basic concepts needed to understand what a laser is and how it works are contained in the word LASER itself. The word is an acronym for *Light Amplification by Stimulated Emission of Radiation*. Stimulated emission, together with absorption and spontaneous emission, is one of the three processes that can happen when an atom interacts with light. Let us now take an ensemble of two-level systems. We will now have N_g atoms in the ground state and N_e in the excited state. The light field is resonant and has a spectral energy density $\rho(\omega_{eg})$. Let us now describe the three processes differently from what has been done in Chapter 2, namely using Einstein's coefficients.

- The *absorption rate* is proportional to the number of atoms in the ground state, the field energy density, and the Einstein B-Coefficient B_{ge}. We get the following equation for the ground state atoms:

$$\dot{N}_g = N_g B_{ge} \rho(\omega_{eg}). \tag{3.1}$$

- The *spontaneous emission* is given just by the spontaneous decay of atoms in the excited state. We can describe the number of excited state atoms with the following

expression:

$$\dot{N}_e = -A_{eg} N_e, \tag{3.2}$$

where A_{eg} is called Einstein A-Coefficient. The equation describes just an exponential decay with lifetime $\tau_{eg} \equiv 1/A_{eg}$.

- In the *stimulated emission* process, the photon is emitted with the same direction, polarization, and phase of the incident one. In this case:

$$\dot{N}_e = N_e B_{eg} \rho(\omega_{eg}). \tag{3.3}$$

Applying the detailed balance principle and expressing the level occupation numbers with Boltzmann factors, we get an equation for the energy density as a function of Einstein's coefficients:

$$\rho(\omega_{eg}) = \frac{A_{eg}/B_{eg}}{\frac{B_{ge}}{B_{eg}} \exp(\frac{\hbar\omega_{eg}}{k_B T}) - 1}. \tag{3.4}$$

Comparing Eq. (3.4) with the Planck distribution gives expressions for the coefficients:

$$B_{eg} = B_{ge} \qquad \frac{A_{eg}}{B_{eg}} = \frac{\hbar\omega_{eg}^3}{\pi^2 c^3}. \tag{3.5}$$

These can be applied to a generic field, not only for blackbody radiation since the coefficients are constants.

Amplification

Let us now think about what happens when a light beam travels through the ensemble. Depending on the population difference $N_e - N_g$, it will either be amplified or damped. The change in energy per time in a frequency interval is given by the following equation:

$$(n_e - n_g) B_{eg} g(\omega) \frac{I(z)}{c} A dz \hbar\omega_{eg}, \tag{3.6}$$

where n_i are the population densities, $g(\omega)$ takes into account the atomic transition linewidth, and A is the area addressed by the laser, over which we assume constant density of intensity. Intensity can be expressed as a function of position z:

$$I(z) = I_0 \exp\left[(n_e - n_g) B_{eg} g(\omega) \frac{\hbar\omega_{eg}}{c} z\right] = I_0 \exp(\gamma_g z), \tag{3.7}$$

with γ_g the gain coefficient. If the gain is positive, intensity increases. This gives a condition on the atomic level occupancy: $N_e - N_g > 1$. For a two-level system, population inversion cannot be achieved: the excited state population given in Eq. (2.5) cannot go above $\frac{1}{2}$. We need a process that pumps the medium.

Amplifer Bandwidth and Phase Shift The gain coefficient is frequency dependent due to the spectral density $g(\omega)$. If, for example the spectral density is given by a Lorentzian function, centered on resonance frequency ω_0, then

$$g(\omega) = \frac{\Delta\omega}{(\omega - \omega_0)^2 + (\Delta\omega/2)^2}. \tag{3.8}$$

The gain coefficient will then also be Lorentzian with the same width $\Delta\omega$.

The frequency dependence of the gain makes the medium dispersive and produces a frequency-dependent phase shift. This phase shift is related to the gain coefficient by the Kramers-Kronig relations. Let us take again the Lorentzian case, then the phase shift will be given by:

$$\phi(\omega) = \frac{\omega - \omega_0}{\Delta\omega}\gamma_g(\omega). \tag{3.9}$$

Amplification Source We said that to have amplification we need population inversion. For this to happen we need some pumping mechanism. The pumping can be optical, electrical or chemical. We can write rate equations that describe the change in the levels' population. We are not longer in equilibrium so we need to take the decay times into account. Suppose we have two levels: 1 and 2, with lifetime τ_1 and τ_2, respectively. The lifetime τ_2 will be given by different contributions: the decay to level 1, radiative or non-radiative $\tau_{21}^{-1} = \tau_{\text{sp}}^{-1} + \tau_{\text{nr}}^{-}1$, and the decay to other levels τ_{20}. If we allow the system to reach a steady state, all atoms will decay to other levels. We can maintain population of levels 1 and 2 if we excite higher levels that would then decay to 2. This can be done with pumping rates R_1 and R_2. We can write rate equations including the presence of radiation with the probability density of stimulated emission W_i, which is equal to $B_{eg}g(\omega_{eg})$, in case of light with a spectral energy density broader than the atomic linewidth.

$$\begin{aligned} \frac{dN_2}{dt} &= R_2 - \frac{N_2}{\tau_2} - N_2W_i + N_1W_i \\ \frac{dN_1}{dt} &= -R_1 - \frac{N_1}{\tau_1} + \frac{N_2}{\tau_{21}} + N_2W_i - N_1W_i. \end{aligned} \tag{3.10}$$

In the steady-state case, the population difference N is given by:

$$N = \frac{N_0}{1 + \tau_s W_i}, \tag{3.11}$$

with $\tau_s = \tau_2 + \tau_1(1 - \tau_2/\tau_{21})$ the saturation time constant and N_0 the steady-state population difference in absence of radiation:

$$N_0 = R_2\tau_2\left(1 - \frac{\tau_1}{\tau_{21}}\right) + R_1\tau_1. \tag{3.12}$$

We already mentioned that a two-level system cannot provide the conditions for lasing. Common lasers use four-level or three-level schemes, as shown in Fig. 3.1.

(a) **(b)**

Figure 3.1 Level schemes with pump transitions and decays. The lasing transition is the one with W_i^{-1}. (a) Four-level scheme. Atoms quickly decay to the ground state 0 depleting level 1. At the same time, they get pumped to 2 via level 3. Level 2 is long lived, which produces population inversion. (b) Three-level scheme. Level 1 is now the ground state. Level 2 is again populated via level 3.

We have seen that the gain coefficient is a function of the population difference N, which depends on W_i. This is in turn, in its general form, a function of the photon-flux density ϕ:

$$W_i = \phi \frac{\lambda^2}{8\pi\tau_{\mathrm{sp}}} \rho(\nu), \tag{3.13}$$

with $\rho(\nu)$ the spectral energy density, so we can write :

$$N = \frac{N_0}{1 + \phi/\phi_s(\nu)}, \tag{3.14}$$

with:

$$\frac{1}{\phi_s(\nu)} = \frac{\lambda^2 \tau_s}{8\pi\tau_{\mathrm{sp}}} \rho(\nu). \tag{3.15}$$

This gives the final result for the gain:

$$\gamma(\nu) = \frac{\gamma_0(\nu)}{1 + \phi/\phi_s(\nu)}, \tag{3.16}$$

with

$$\gamma_0(\nu) = N_0 \frac{\lambda^2}{8\pi\tau_{\mathrm{sp}}} \rho(\nu). \tag{3.17}$$

Feedback

So far we have just looked at the gain amplification, but, to have a laser we need some feedback process. This can be achieved by placing the active medium inside a resonator. Let us take a Fabry-Perot cavity made up of two mirrors at distance d. Light traveling across the cavity acquires a phase shift given by the wavevector. Moreover, the cavity is a source of loss; we can describe the loss for every round trip as:

$$\exp(-2\alpha_r d) = R_1 R_2 \exp(-2\alpha_s d), \tag{3.18}$$

where R_j is the intensity reflectance of the j-th mirror, α_s is the attenuation coefficient, and α_r is the total effective loss coefficient. We could also talk about photon lifetime in terms of $\tau_p = 1/\alpha_r c$, where $c = c_0/n$ is the speed of light in the cavity medium.

The resonator additionally puts a constraint on light frequency in the sense that it can sustain only those frequencies that correspond to a phase shift multiple of 2π.

$$\nu_q = q\nu_F = q\frac{c}{2d}, \qquad q = 1, 2, \ldots, \tag{3.19}$$

where ν_F is the resonator mode spacing. The spectral width of the modes is given by $\delta\nu \sim \nu_F \mathscr{F}$, where $\mathscr{F}$ is the so-called finesse of the resonator. For low losses:

$$\mathscr{F} = \frac{\pi}{\alpha_r d} = 2\pi\tau_p\nu_F. \tag{3.20}$$

For the oscillation to happen we need:

$$\gamma_0(\nu) > \alpha_r, \tag{3.21}$$

which gives a condition for the population difference $N_0 > N_t = \frac{8\pi}{\lambda^2 c}\frac{\tau_{\mathrm{sp}}}{\tau_p}\frac{1}{\rho(\nu)}$. The population difference N_t is the threshold population difference.

Lasing still requires another condition on the phase. Only light that after a round-trip is in phase with new light entering the resonator will build up, that is why the phase must be a multiple of 2π:

$$2kd + 2\phi(\nu)d = 2\pi q, \qquad q = 1, 2, \ldots \tag{3.22}$$

Spectral Distribution

The spectral distribution of the laser light is constrained by the atomic lineshape and by the cavity modes. The gain condition is satisfied for a band B proportional to the atomic linewidth and the factor $\gamma_0(\nu_{eg})/\alpha_r$. The resonator than allows just modes with full width at half maximum (FWHM) $\delta\nu$, so the number of allowed modes can be ap-

proximated by

$$M \sim \frac{B}{\nu_F}. \tag{3.23}$$

What we discussed so far is valid for all lasers. We want now to quickly describe diode lasers, which we will use throughout this thesis.

3.1.2 Laser Diodes

In semiconductors, light can be emitted as a result of electron-hole recombination. This does not mean that a semiconductor can glow by itself; we still have to produce an active region. For this purpose, the concept of doping is central. Doping a material means introducing impurities to alter its properties. There are two types of doping. We can either produce a material with an excess of electrons or a material lacking electrons. In the first case we call the material *n-doped*, in the second, *p-doped*. The p-doped case can also be seen as an excess of holes. The basic element that we can construct is the *p-n junction*. This is the basic element of every laser diode: an n-doped substrate onto which a p-doped layer is grown. We can then create our active region by applying a current between the two layers.

P-n Junction

As for every laser, we need population inversion. To understand what this means in the semiconductor case, let us have a look at the p-n junction.

To describe the system, we need to work within the framework of band theory. When we look at the allowed wave functions for electrons in a periodic lattice, the atomic orbitals of each atom overlap. Due to the Pauli principle, every atomic orbital gets split into N molecular orbitals, where N is the number of atoms. In a solid, this means that the number of orbitals is very large, and the energy levels are so close that we can describe them as a continuum: the band. Not allowed energy values are called bandgaps. The last occupied band is called *valence band*, the first unoccupied band is called *conduction band*. The band description allows distinguishing between conductors and insulators. An insulator has a bandgap so large that electrons in the valence band cannot be excited to the conduction band; this prevents currents from flowing. In contrast, in a conducting material, electrons are free to move. A semiconductor shows an insulating behavior at 0 K, but the bandgap is small enough to become conductive at higher temperatures.

In a semiconductor, we can have two types of bandgap:

- Direct bandgap: this type of band has the conduction band edge at the same position in $\mathbf{k}$-space as the valence band edge.
- Indirect bandgap: the edges do not have the same position, and we need a phonon to produce the transition from the valence to the conduction band.

Another characteristic of semiconductors is the position of the Fermi energy E_F. It describes the energy we need to add an additional electron at $T = 0$, and, for semiconductors, it lies in the bandgap.

We said that we need population inversion, so we need a region with more electrons in the conduction band than in the valence one. If we bring p- and n-doped semiconductors together, we have a density gradient between holes and electrons, which leads to diffusion until a steady-state is reached and the Fermi level is equilibrated. Electrons moving from the n-doped side to the p-doped side leave a positively charged region; the opposite happens for the holes in the p-doped region. The result is a potential difference that prevents further diffusion. If we apply a forward voltage, we can overcome this barrier, and current can flow. When the voltage matches the bandgap, a region is formed, where we have electrons in the conduction band and holes in the valence band: the required population inversion. Light can then cause recombination of electrons and holes via stimulated emission.

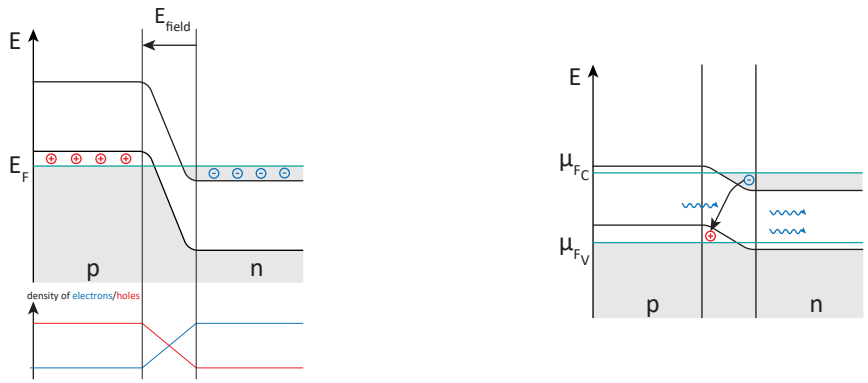

(a) **(b)**

Figure 3.2 P-n junction schemes. (a) Band structure of a p-n junction with no forward-bias voltage applied, showing a constant Fermi level μ_F. (b) The application of a forward bias voltage produces population inversion and thus enables electron-hole recombination.

It is clear that recombination in a direct bandgap is more efficient. A way to increase the efficiency further is the use of *heterojunctions*, meaning the use of different semiconductors for the p- and n-doped sides. Using two different materials produces discontinuities in the bands. If we use two discontinuous junctions, we obtain a heterostructure, which is shown in Fig. 3.3. The discontinuities bound the active region. When we apply a forward voltage, we produce charge confinement in this region. In this kind of structure, it is possible to engineer the active region size, which means that, for the same current as

for the p-n junction, we can produce higher carrier density. As we have seen, the gain depends on the population density, so it can be higher in this case.

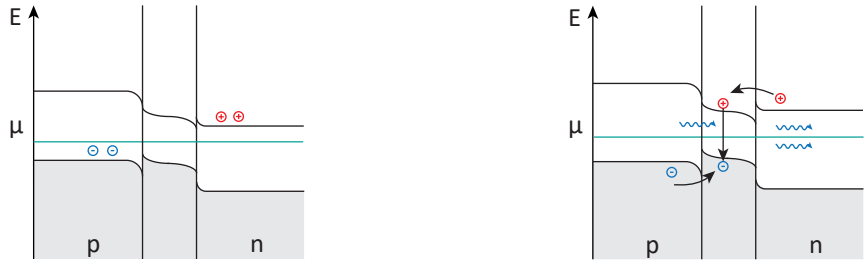

(a) **(b)**

Figure 3.3 Heterostructure schemes. (a) Band structure of a heterostructure with no forward-bias voltage applied. (b) The application of a forward bias voltage produces charge confinement in the active region.

If we further reduce the size of the active region and approach the de Broglie wavelength, we obtain the so-called *quantum well*. As before, the reduced width increases the gain and consequently reduces the lasing threshold. An additional feature is that the layer is thin enough to form structures even with materials of different lattice constants, which in other conditions would produce defects. Moreover, the gain values are less sensitive to temperature. For semiconductors in general, the gain decreases with increasing temperatures. For quantum wells, the inversion is less affected than the bulk case.

Blue Laser Diodes

We will use three different blue laser diodes. Therefore, we would like to spend a few words on how these are made. The following discussion is based on Ref. [50].

To build blue light emitting diodes (LEDs) and LDs, both II-VI materials such as ZnSe, SiC, and III-V nitride semiconductors such as GaN have been investigated. Devices based on II-VI materials showed short lifetimes, which makes the commercialization difficult. The other options are III-V nitride semiconductors as GaN or AlGaInN. They have a wurtzite crystal structure and a direct energy gap. The bandgaps are suitable for

emitting blue light; GaN has, for example, an energy gap of about 3.4 eV, corresponding to a wavelength of 365 nm [50].

The first difficulty in designing the blue LDs was the identification of the substrate on which to grow the GaN. The reason is that it is challenging to find a material with a similar lattice constant. If a mismatch occurs, the GaN grows with defects. Defects can then produce distortions in the active region. The two best candidates are Spinel ($MgAl_2O_4$), which has a 9.5% mismatch, and sapphire, with a 13% mismatch. II-VI materials should apparently work better since they have similar crystal structure and lattice constant as gallium arsenide. However, these materials are more fragile. GaN related compounds are grown at higher temperatures (over 1000°C) and can withstand annealing and high-temperature processing. This also enables the fabrication of ohmic contacts. Good ohmic contacts are required to prevent heating of the diode. The first GaN growth on sapphire was demonstrated by Akasaki in 1986 using metalorganic vapor-phase epitaxy (MOVPE). Different AIN buffers layers served as adapters between the different crystal structures [51]. Later, Nakamura *et al.* developed a new technique that led to improved crystal growth: the two-flow metal organic chemical vapor deposition (TF-MOCVD), which exploits a second gas jet of nitrogen and hydrogen to push reactants towards the growth surface [52].

Another difficulty, which has now been understood and solved, was the p-doping of GaN (or AlGaN). A first p-type doped conducting GaN was produced by irradiation with low energy electrons (LEEBI) by Akasaki *et al.* [53]. This process was later clarified by Nakamura, and high-conductivity was achieved in Mg-doped p-type GaN [54]. Magnesium acceptors get deactivated by atomic hydrogen produced by ammonia gas used during the growth. The same method has been applied to heterostructures and quantum wells.

At first, researchers were able to produce stimulated emission only with optical pumping. The first current-injection III-V nitride based LDs were fabricated by Nakamura *et al.* using InGaN in a multi-quantum-well structure. The laser wavelength was 417 nm. The cavity was formed by etching III-V nitride films.

We just briefly mentioned some issues and characteristics of blue laser diodes. This is still an open field of research. For example, the diode we will use for our 2D MOT is a single mode high power GaN laser diode that became available very recently.

3.2 External Cavity Linear Laser

In this section, we will briefly discuss the laser setup we will use for absorption spectroscopy. The mounting procedure and the laser characterization can be found in Ref. [55]. The laser is a diode laser with linear external cavity (ECDL) with a wide bandwidth interference filter to select the laser wavelength. The main feature of this type of

laser is the decoupling between the feedback mechanism and the frequency selection. This produces a larger tunability than, for example, a Littrow laser [56]. In addition, the optical path is not affected by horizontal length changes of the cavity, so the frequency is more stable.

Our setup is shown in Fig. 3.4. The basic element is a laser diode (Nichia NDB4216), which is collimated through an aspheric lens of focal length $f = 18.4$ mm. This is then followed by the interference filter and another lens focusing the light on the output coupler. These elements are the constituents of the laser cavity. The output is then recollimated by another lens. The elements mentioned are mounted on a monolithic aluminum housing that rests on two Peltier elements. These, together with a thermistor, allow tuning and control of the laser temperature. With the protection board, this housing is placed inside another one, designed to be evacuable thanks to a KF gasket.

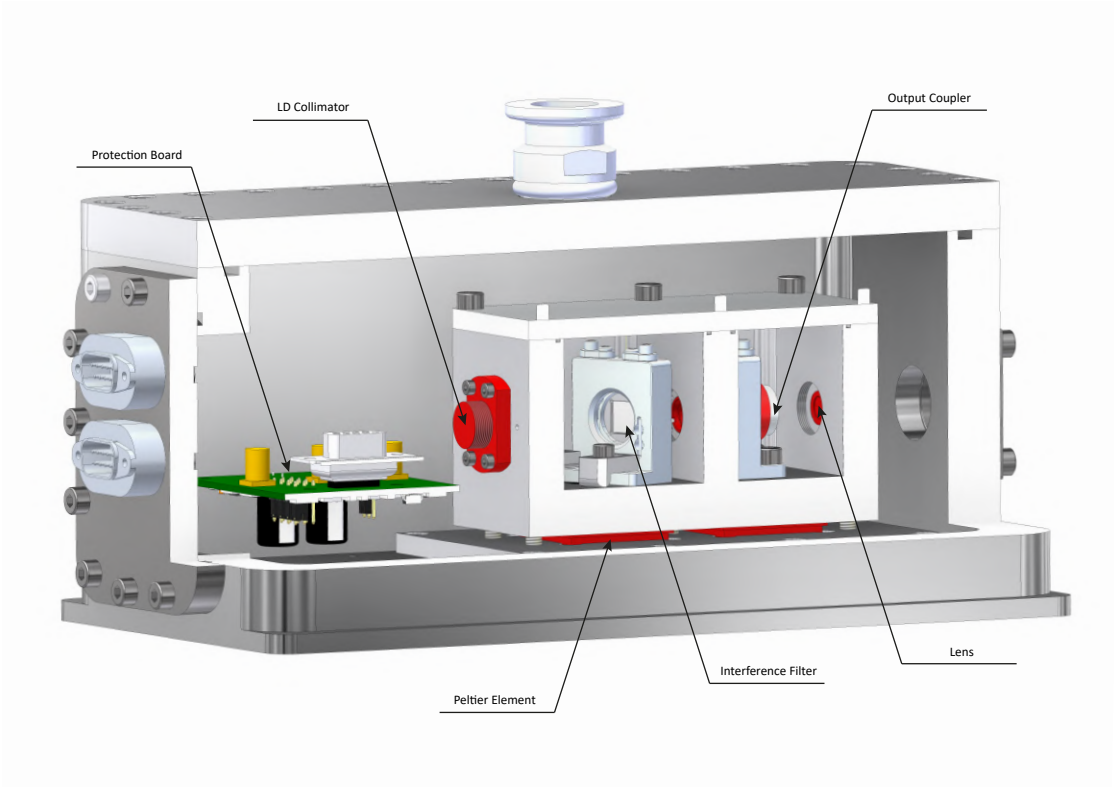

Figure 3.4 ECDL laser render.

A protection board is the circuit included to protect the laser diode from incorrect currents and voltage spikes. Moreover, it minimizes noise sources and acts as an intermediary between the laser diode and the control units from Thorlabs or Toptica that we employ in the lab. The protection board can be used with different types of diodes and control units with some small changes to some resistors in the circuit. For this reason,

we will use it also for the 2D MOT laser and for the Zeeman repump later, although the setups are completely different. Briefly, a series of bypass capacitors (C1-C4) isolates the diode from high-frequency noise, while a Schottky diode (MBRO540) protects against driving currents with the wrong polarity. There is also a relay circuit to protect the laser diode from static electricity when the controller is disconnected. The design also allows DC- and AC-modulation and contains an amplifier circuit for the photodiode embedded with the laser diode, although we will not use those circuits. Further details on the protection board design can be found in Ref. [57].

The characterization of this laser has shown a threshold current of around 18 mA, taking into account the current drawn by the protection board. The Iridian 473 nm bandpass filter has a FWHM of about 3 nm. Another important feature is the laser linewidth, which has to be lower than the $^1S_0 \rightarrow ^1P_1$ one. The linewidth was measured in Ref. [55] in two different ways. Although they produced different results, both showed a linewidth lower than 30.5 MHz. The final requirement for doing absorption spectroscopy is a large mode-hop free tuning range. We need this to be able to measure the entire absorption spectrum of our atomic beam. The frequency is scanned with a piezo. To avoid mode-hops when scanning the piezo, a current is fed forward, which causes the gain spectrum to shift. After the addition of an inverting circuit to the Toptica Sys DC 110 signal, it was possible to obtain a mode-hop free tuning range of 6.8(1) GHz. This was, in practice, difficult to reproduce at every laser operation due to the laser instability. The instability problem has been tackled in Ref. [58], where a new laser housing has been designed.

Still, this laser has all the characteristics we need to perform absorption spectroscopy on our atomic beam. We will now have a look at the laser we will use for the 2D MOT.

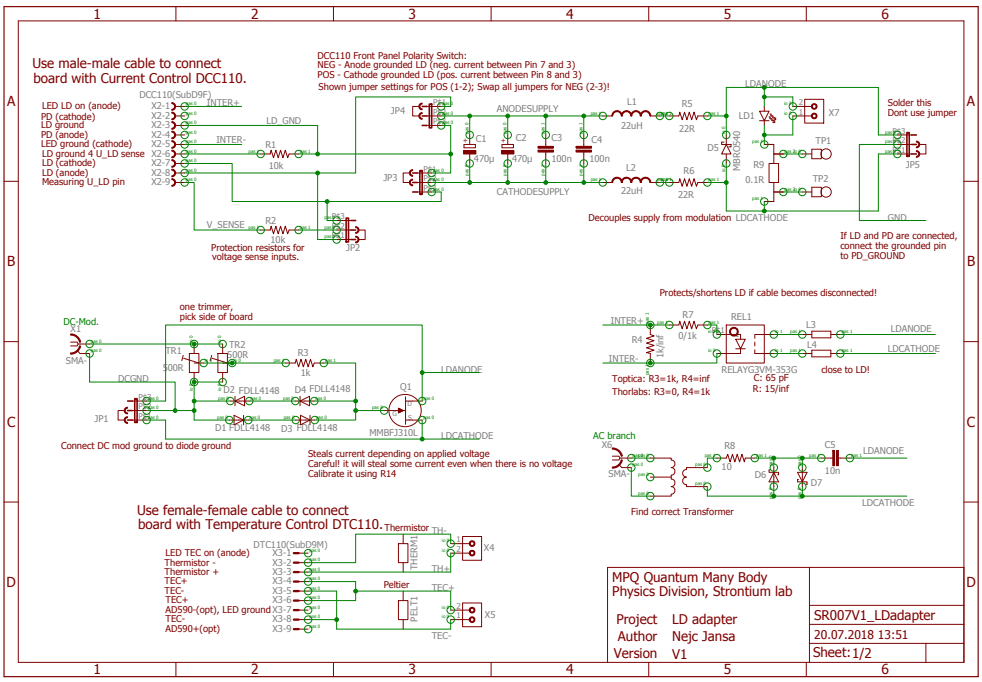

(a)

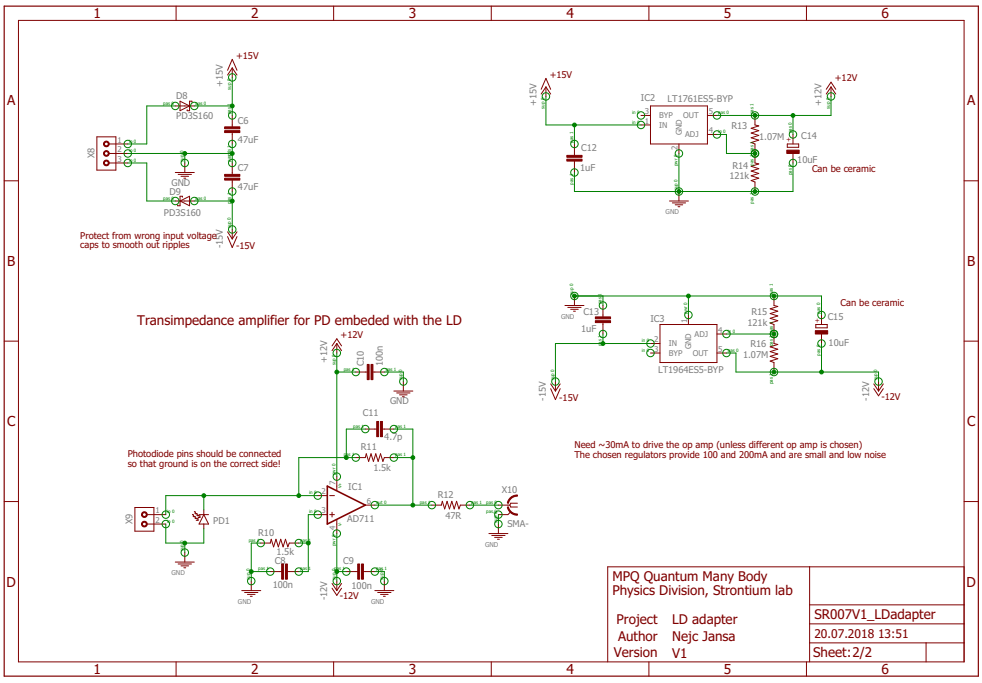

(b)

Figure 3.5 Protection board circuit diagram. (a) LD protection circuit, temperature reading circuit, DC-modulation circuit, and AC-modulation circuit. We will use just the first two. (b) Transimpedance amplifier for the photodiode embedded with the LD.

3.3 Injection Locking

The original idea was to use the ECDL laser also for the 2D MOT beams, but the output power is not high enough, so we built a second laser. This time we used a new Nichia diode, which can output 500 mW of blue light (NDB4916E). The spectrum of this diode is broad, so we decided to use injection locking. The generation of spectrally pure light at 460.86 nm with this diode has already been demonstrated in Ref. [59].

3.3.1 Principle

As already mentioned, the laser diode is broadband. If we seed a so-called slave diode by injecting external light with a narrow linewidth, the slave can emit light with the same properties. For this to happen, the seed light must be stronger than the spontaneously emitted light by the unseeded diode so that the seed gets amplified and the other modes are suppressed. Moreover, the seed light needs to be mode matched to the internal cavity of the slave diode. The less power we want to exploit for the seed, the better the mode-matching has to be.

3.3.2 2D MOT Laser

Setup

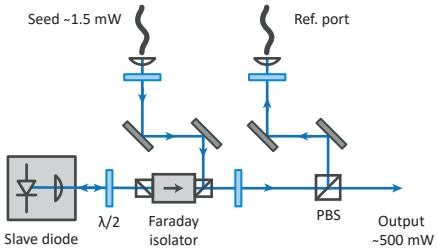

Figure 3.6 Optics setup used for the injection lock module.

The tools we need to build an injection lock setup are shown in Fig. 3.6. After the laser diode, we use an optical isolator. This prevents the backscattered light from coupling back into the laser and thus protects the laser diode. It is made up of three parts: two polarizers, an input and an output one, and a $45°$ Faraday rotator. The light emitted by the slave diode is polarized and then rotated such that it can travel through the second polarizer. On the other hand, light traveling backward will not be transmitted. Seed light is coupled into a fiber and collimated using a Thorlabs collimator (PAF2-A7A). The half-wave plate after the collimator allows tuning the polarization until the seed

light is transmitted through the isolator and reaches the slave diode. To couple the seed light, we use two $0.5''$ mirrors. The other half-wave plate and the polarizing beam splitter (PBS) are used to split some light and couple it to an optical fiber to monitor the lock with an optical spectrum analyzer.

This setup is contained in a compact module built on a custom breadboard and enclosed in acrylic walls to enhance stability. Details on the design of this setup can be found in Ref. [57].

The isolator is from Thorlabs and is designed for 473 nm light, so it has to be optimized for our 461 nm light. We care mostly about the isolation, so we tune this by reversing the isolator and adjusting the output polarizer to minimize the transmission.

Then we align the beams. We first couple the slave light into the seed fiber. Intuitively, the seed light should automatically have a good pointing. When the coupling is reasonably good, we can use the current and temperature controllers to lock the laser. The diode's temperature is read out using a thermistor glued on the laser diode housing and tuned with two Peltier elements. The design of the housing is meant to fit just one Peltier positioned above the laser diode. For our high-current laser diode, we found that one Peltier was not enough to stabilize the temperature when we increased the laser current. For this reason, we positioned a second Peltier underneath the housing to put it in thermal contact with the breadboard. We improved the contact with indium foil. Temperature and current are tuned via a Thorlabs controller (ITC4001). Temperature changes the center wavelength; we can use the temperature controller to move the spectrum towards the seed frequency to help the lock. Two things have to be considered when tuning the temperature. First, we should not exceed 30-35° C since high temperatures reduce the diode's lifetime. Second, we should choose a temperature slightly above room temperature to avoid temperature oscillations. We set it at $26°$ C.
To lock the laser, we then tune the current. The slave can be locked every 30 mA. Another crucial element to get a stable lock and to be able to lock at high currents is the seed power. We found that we need about 1.5 mW to lock the laser at full power.

Laser Characterization

First of all we checked the power vs current curve. The result is shown in Fig. 3.7.

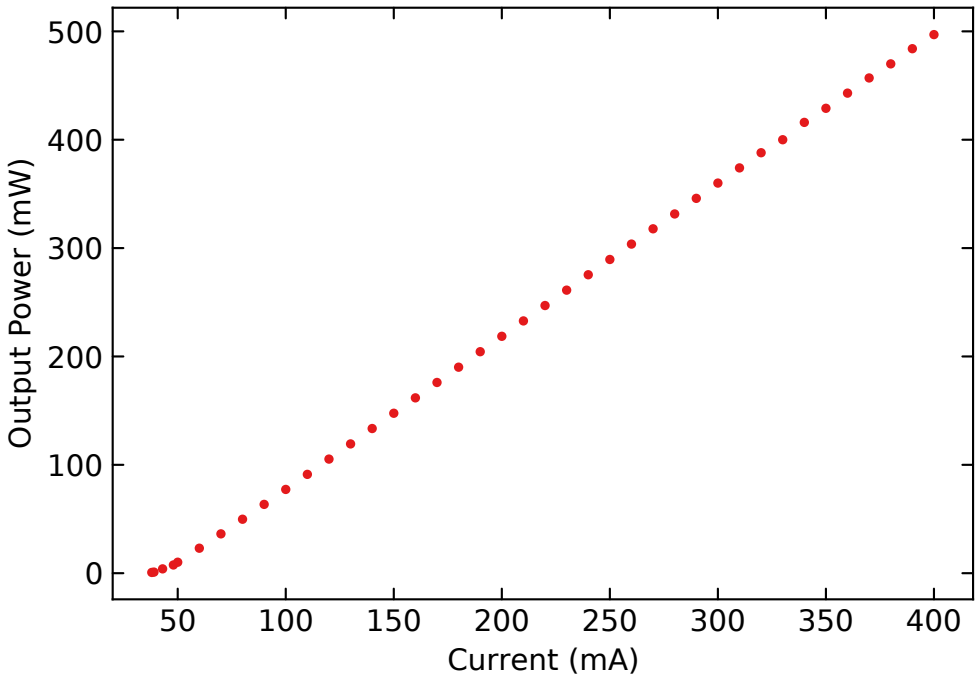

Figure 3.7 Output power of the laser diode in function of the driving current.

In the next figure we can see the effect of injection locking. In Fig. 3.8 (a) we see the unlocked laser. In (b) the laser has been pulled towards the seed wavelength.

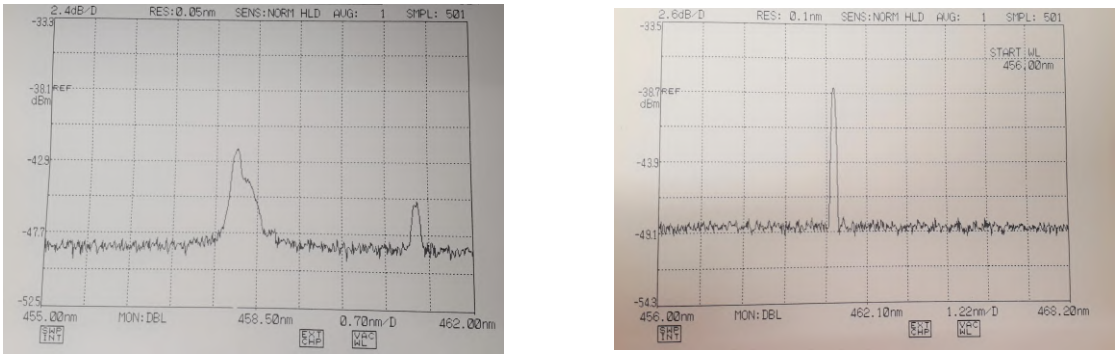

(a) **(b)**

Figure 3.8 Example of laser spectra. (a) Spectrum of the bare diode. (b) Spectrum of the laser after injection locking.

This is the laser that we will use to produce the 2D MOT beams. We postpone the discussion on the seed light to Chapter 6 where we will describe the whole laser setup.

In this chapter, we briefly discussed the working principle of lasers and described the lasers that we will use for the main topic of this thesis. We also built another laser for the Zeeman repump transition, described in Appendix B. We will now move to the discussion on oven spectroscopy. This will provide us with the tools to understand the results given by our 2D MOT.

Chapter 4

Oven Spectroscopy

Before looking at the effect of our 2D MOT on the atomic beam, we need to characterize the beam effusing from our oven. This will be done with absorption spectroscopy and will allow us (i) to characterize better the improvement caused by the 2D MOT, and (ii) to understand what needs to be changed in the next generation of our oven. In this chapter, we will first describe the principle of absorption spectroscopy, following the discussion in Ref. [45], and then move to our setup.

4.1 Absorption Spectroscopy

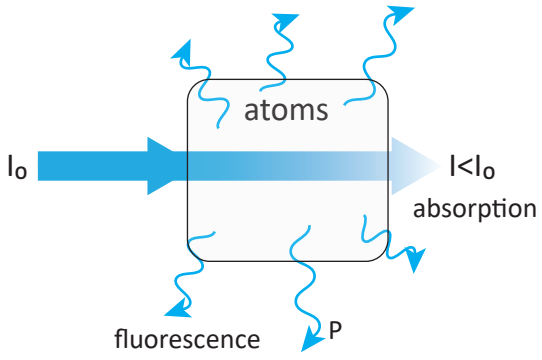

Figure 4.1 The intensity of a laser beam sent through an atomic cloud is reduced due to the atoms' absorption. The corresponding energy is then re-emitted in the form of fluorescence light.

When doing absorption spectroscopy, we look at the reduction of intensity in a beam when traveling across an atomic sample. This decrease occurs since light is absorbed and then re-emitted in random directions generating a fluorescence signal. The rate of energy P emitted for N atoms is given by the absorption rate obtained in Eq. (2.7):

$$P = \hbar\omega_0 N\Gamma_{sc} = \hbar\omega_0 N \frac{s_0\Gamma/2}{1+s_0+(2\Delta/\Gamma)^2}. \tag{4.1}$$

At equilibrium, this corresponds to the energy absorbed, so the intensity reduction is:

$$dI = -n\hbar\omega_0 \frac{s_0\Gamma/2}{1 + s_0 + (2\Delta/\Gamma)^2} dz, \tag{4.2}$$

where n is the atomic beam density. The intensity information is contained in the saturation parameter s_0; for low saturation, the expression reduces to

$$dI = -n\hbar\omega_0 I \frac{\Gamma}{2I_s} \frac{1}{1 + (\frac{2\Delta}{\Gamma})^2} dz = -\alpha_0 I dz, \tag{4.3}$$

where α_0 is the absorption coefficient. Integration leads to the *Beer-Lambert law* describing the absorption of an initial intensity I_0:

$$I(z) = I_0 e^{-\alpha_0 z}. \tag{4.4}$$

Proper treatment should take the position dependences into account. We can rewrite the formula in terms od the optical depth (OD) of the atomic cloud

$$I = I_0 e^{-\mathrm{OD}}, \tag{4.5}$$

where

$$\mathrm{OD} = \int_0^L \sigma n dz. \tag{4.6}$$

Here L is the length traveled by the light across the atomic sample, and σ is the scattering cross section

$$\sigma = \frac{\sigma_0}{1 + \frac{4}{\Gamma^2}(\Delta)^2}. \tag{4.7}$$

The resonant scattering cross section is given by $\sigma_0 \equiv 3\lambda^2/2\pi$. We expect a Lorentzian dip in the frequency of FWHM Γ. The difficulty resides in the velocity distribution, which is a priori unknown. This distribution follows from the angular distribution, which is strictly dependent on the source characteristics. For this reason, we will postpone the discussion to Section 4.2, where we will deal with the real setup and how this affects the atomic beam. Before doing that, let us discuss some broadening mechanisms that could perturb our measurement.

4.1.1 Broadening Mechanisms

Doppler Broadening

As discussed in Section 2.3, atoms in motion see the laser frequency-shifted due to Doppler shift. This leads to a broadening of the absorption profile for different reasons, the first one being that the atomic density can be a function of velocity. The second is

that the cross section has to be modified to contain the Doppler shift:

$$\sigma' = \frac{\sigma_0}{1 + \frac{4}{\Gamma^2}(\Delta - \mathbf{k}\cdot\mathbf{v})^2}. \tag{4.8}$$

We still do not know the actual velocity and density distributions. However, even just from Eq. (4.8), it is clear that the velocity dependence leads to a frequency distribution.

Power Broadening

Another broadening effect is related to power and saturation. We already mentioned the effect that an increasing saturation has on the scattering rate in Section 2.3. This broadening gets translated here into the scattering cross section. In practice the FWHM scales as $\Gamma\sqrt{1+s_0}$. We will try to avoid this broadening by operating at 10% or lower of $I_s \sim 40.6\ \mathrm{mW/cm^2}$.

Transit-time Broadening

The so-called transit-time broadening could give another significant contribution to broadening. When atoms travel through a laser beam of waist w_0, they experience an electric field for a time $T = w_0/v$. The laser beam has a Gaussian distribution

$$E(t) = E_0 e^{-\frac{r^2}{w_0}} \cos(\omega_0 t), \tag{4.9}$$

where r is the radial distance. What matters here is the frequency spectrum given by the Fourier transform of the field. The Fourier transform of a Gaussian is again a Gaussian so:

$$I(\omega) \propto \exp\left[-\frac{w_0(\omega-\omega_0)}{2v\sqrt{2}}\right]. \tag{4.10}$$

The result is a Gaussian with a FWHM$= \frac{4v}{w_0}\sqrt{2\ln 2}$.

4.2 Setup Description and Atomic beam model

In the previous section, we discussed the working principle of our measurement procedure. We saw that we require more information about the atoms' angular distribution to fully characterize the atomic beam. To do this, we will briefly discuss our setup and a model for the atomic beam. For a better insight into the design and motivation of our setup, see Appendix A.

4.2.1 Setup

Let us have a look at our setup. Our atomic source is an atomic oven where strontium is heated inside a crucible up to 700°C. The atoms then effuse from a hexagonal nozzle made up of microchannels of inner diameter $200\ \mu$m and length 10 mm. The whole setup

is shown in Figure 4.2. In the vacuum chamber, the oven is followed by a first cross with four CF63 viewports that gives enough space for spectroscopy and later to build the 2D MOT. Another cross with two CF40 viewports follows this cross. The second cross serves again for spectroscopy and allows estimating the beam divergence, especially with the aid of a razor blade mounted inside the tube between the two crosses. This razor blade is fixed on a translation stage and allows covering the atomic beam thanks to a micrometer screw.

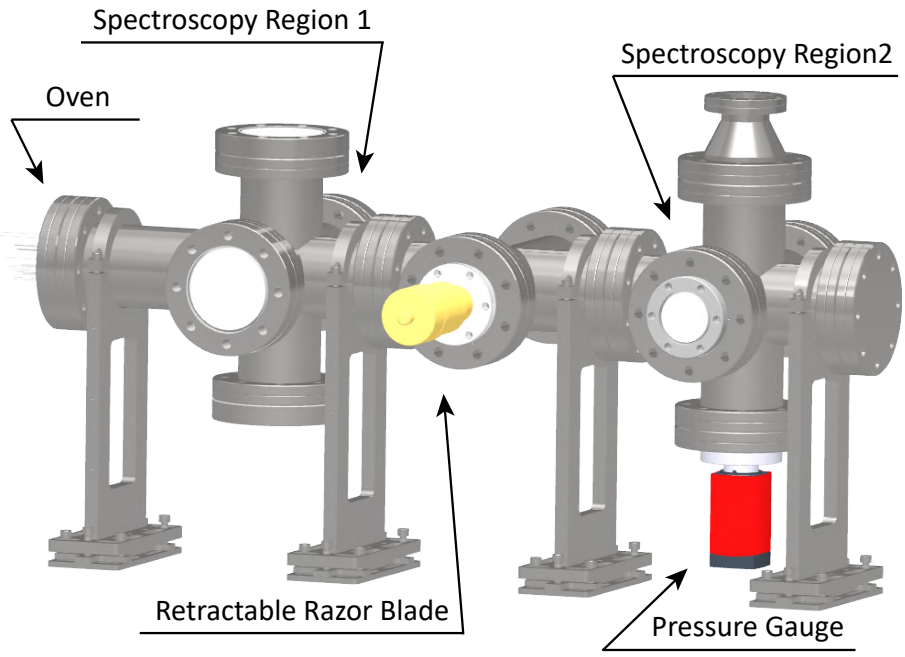

Figure 4.2 Render of the vacuum chamber used to measure the beam parameters. We will do spectroscopy in two regions. Additionally, we will build a 2D MOT in the first one. Between the two crosses, we have a retractable razor blade to cut the atomic beam. A pressure gauge allows monitoring of the chamber's vacuum.

4.2.2 Atomic Beam Model

For the purpose of modeling the atomic beam, the focus is the collimating action done by the microchannels. These microcapillaries exhibit some surface roughness, which makes an atom that hits the wall scatter in all directions with the same probability. In this case, the intensity of atoms scattered at an angle θ is given by Lambert's cosine law: $I \cos\theta d\Omega dA$. This implies that atoms with an angular direction that makes them hit the capillary as soon as they get in, have a small chance to get out on the opposite side. The effect of this is that atoms that make it are those that were already going straight. That is why the microchannels act as collimators and define the distribution of atomic speeds.

The result is the modified Maxwell-Boltzmann distribution [60, 61]:

$$f(v) = \frac{2v^3}{a^4} e^{-\frac{v^2}{a^2}}, \tag{4.11}$$

where $a = \sqrt{\frac{2k_B T}{m}}$. We will probe the beam with a perpendicular light beam, so we still miss the angular velocity distribution than we need for the factor $-\mathbf{k} \cdot \mathbf{v}$ appearing in the cross section of Eq. (4.8).

Angular Distribution

The first question that we would like to answer is: can we neglect collisions between the atoms? In principle, our vacuum is high enough to describe the system as being in the molecular flow regime. This means that the density is low enough so that we can neglect collisions. Is this approximation valid? Let us have a look at the parameter that differentiates between the different flow regimes: the *Knudsen number* Kn. This number is a dimensionless quantity given by the ratio of the mean free path and a characteristic dimension, which is the atomic size in our case. If $\mathrm{Kn} \gg 1$, we are in the molecular regime. If it is lower than 0.1, the flow becomes viscous, and we have to apply the Navier-Stokes equations. Between these two regimes, we have the intermediate flow regime. The Knudsen number is

$$\mathrm{Kn} = \frac{\lambda_{MF}}{L} = \frac{k_B T}{\pi \sqrt{2} d^2 p L}, \tag{4.12}$$

where $d = 498$ pm is the van-der-Waals diameter of strontium, T is the temperature in units of K, $p = 10^{10.255 - \frac{8324}{T}}$ is the vapor pressure of strontium in units of Pa [57], and L is the capillary length. The dependence of the Knudsen number on temperature is shown in Figure 4.3.

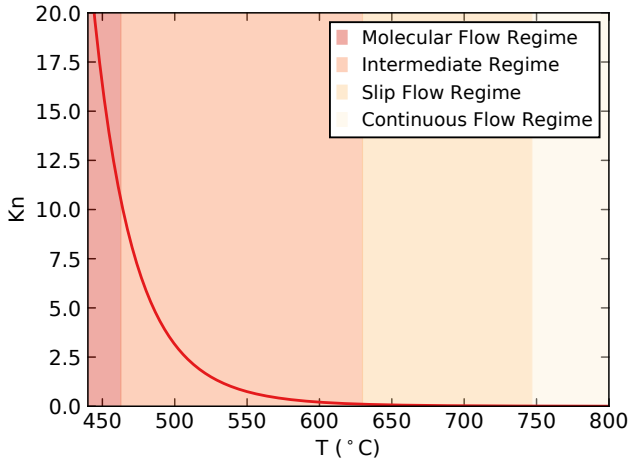

Figure 4.3 Flow regimes as a function of temperature. The molecular flow is usually defined to be the one for $\mathrm{Kn} > 10$. Between 10 and 0.1, we have the intermediate regime. Below that, we have the slip flow and the continuous flow, where the Navier-Stokes equations have to be applied.

Molecular Flow Regime In the molecular flow regime, we assume that atoms hitting the walls of the capillaries follow Lambert's cosine law. Additionally, the rate at which they strike a unit area of a wall at a distance z from the entrance decreases linearly with the capillary length [62]. Let us then take a single microchannel. Given the capillary radius r, the scenarios are two:

- The entrance angle is $\theta < \arctan\left(\frac{2r}{L}\right)$ and the atom travels through the tube without hitting the wall.
- The angle is $\theta \geq \arctan\left(\frac{2r}{L}\right)$, and the atom strikes the wall.

If we define the parameter $q := \left(\frac{L}{2r}\right)\tan(\theta)$ then the angular distribution is:

$$j(\theta) \equiv \begin{cases} \alpha\cos(\theta) + \frac{2}{\pi}\cos(\theta)\left[(1-\alpha)R(q) + \frac{2}{3q}(1-2\alpha)(1-(1-q^2)^{3/2})\right], & \text{if } q \leq 1 \\ \alpha\cos(\theta) + \frac{4}{3\pi q}(1-2\alpha)\cos(\theta), & \text{if } q \geq 1 \end{cases} \tag{4.13}$$

with

$$R(q) = \arccos(q) - q\sqrt{1-q^2}, \tag{4.14}$$

$$\alpha = \frac{1}{2} - \frac{1}{3\beta^2}\left(\frac{1-2\beta^3+(2\beta^2-1)\sqrt{1+\beta^2}}{\sqrt{1+\beta^2}-\beta^2\mathrm{arsinh}(\frac{1}{\beta^2})}\right), \tag{4.15}$$

and $\beta = 2r/L$ is the aspect ratio of the microcapillary. This is calculated in Ref. [63]. In this regime, the distribution depends only on the capillary aspect ratio β. How β influ-

ences the atomic beam divergence is shown in Fig. 4.4. As β gets larger, the distribution gets broader, and for $\beta \to \infty$ it approaches the cosine distribution.

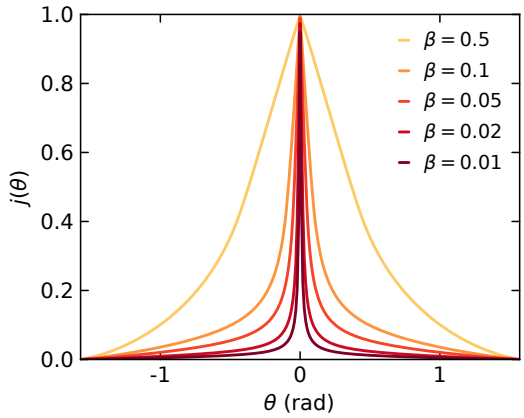

Figure 4.4 Molecular flow regime angular distribution as a function of the aspect ratio β. The distribution gets broader for higher aspect ratios, meaning for shorter microcapillaries.

Intermediate Regime In this regime, the cosine law is still valid, but now we have to consider the interatomic collision rate, which depends on the density profile inside the capillaries [64]

$$n(z) = n_s \left[\xi_1 - (\xi_1 - \xi_0)\frac{z}{L}\right] \tag{4.16}$$

With additional assumptions, which can be found in Ref. [63], we get a complex expression for the angular distribution, containing a temperature dependence in the form of the Knudsen number.

$$j(\theta) \equiv \begin{cases} \frac{2}{\sqrt{\pi}}\xi_0 \cos(\theta)\frac{e^{\delta'^2}}{\delta'}\left[\frac{R(q)}{2}\left(\operatorname{erf}\left(\delta'\frac{\xi_1}{\xi_0}\right) - \operatorname{erf}(\delta') + F(\xi_0,\xi_1,\delta')\right) + S(q)\right] + \xi_0\cos(\theta), & \text{if } q \le 1 \\ \xi_0\cos(\theta) + \frac{2}{\sqrt{\pi}}\xi_0\cos(\theta)\frac{e^{\delta'^2}}{\delta'}S(1), & \text{if } q \ge 1 \end{cases} \tag{4.17}$$

with

$$S(q) = \int_0^q \sqrt{(1-t^2)}\left[\operatorname{erf}\left(\delta'\left(1 + \frac{t(\xi_1-\xi_0)}{q\xi_0}\right)\right) - \operatorname{erf}(\delta')\right] dt, \tag{4.18}$$

$$F(\xi_0,\xi_1,\delta') = \frac{2}{\sqrt{\pi}}\delta'\frac{(1-\xi_1)}{\xi_0}e^{-\left(\frac{\delta'\xi_1}{\xi_0}\right)^2}, \tag{4.19}$$

$$\delta' = \frac{\delta}{\sqrt{\cos(\theta)}}, \tag{4.20}$$

$$\delta = \frac{\xi_0}{\sqrt{2\mathrm{Kn}(\xi_1-\xi_0)}}. \tag{4.21}$$

Let us compare the two regimes via Fig. 4.5.

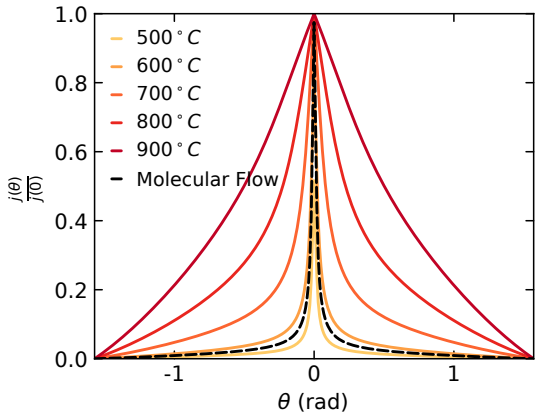

Figure 4.5 Comparison of the angular distribution for $\beta = 0.02$ in case of molecular and intermediate flow regime. The intermediate case had to be renormalized since the centerline intensity is no longer unity as it was in the molecular flow case. As we can see, the distribution gets broader for increasing temperature since collisions become more likely.

Transmission Spectra

Now that we have an expression for the angular distribution, we can write the final formula for the transmission spectra. The transmission is given by the Beer-Lambert law in Eq. (4.4) with the scattering cross section given by:

$$\sigma = \frac{2\sigma_0}{a^4}\int_0^\infty dv \int_0^{\pi/2} d\theta \sin\theta \int_0^{2\pi} d\phi \frac{j(\theta)v^3 e^{-\frac{v^2}{a^2}}}{1+\frac{4}{\Gamma^2}(\Delta + kv\sin\theta\cos\phi)^2}. \tag{4.22}$$

The expression considers the velocity distribution, the angular distribution, and the single atom cross section. We can simplify the form with the introduction of the parameters $\rho := \frac{v}{a}$, $\delta := \frac{2\Delta}{\Gamma}$ and $\eta := \frac{2ka}{\Gamma}$. Taking also the expression for the angular distribution into account:

$$\begin{aligned}\sigma =& 2\sigma_0 \int_0^\infty d\rho \left(\int_0^{\arctan(\beta)} d\theta \sin\theta \int_0^{2\pi} \frac{j_{q\leq 1}(\theta)\rho^3 e^{-\rho^2}}{1+(\delta+\eta\rho\sin\theta\cos\phi)^2} \right. \\ &\left. + \int_{\arctan(\beta)}^{\pi/2} d\theta \sin\theta \int_0^{2\pi} \frac{j_{q\geq 1}(\theta)\rho^3 e^{-\rho^2}}{1+(\delta+\eta\rho\sin\theta\cos\phi)^2} \right).\end{aligned} \tag{4.23}$$

We now have all the tools to fit the spectroscopy signal and extrapolate information about the atomic flux and total flow rate. The only free parameter is the density n from which we can calculate the atomic flux:

$$F = n\bar{v}, \tag{4.24}$$

and the total flow rate

$$\dot{N} = \frac{\pi R_{\mathrm{cap}}^2}{2} F N_{\mathrm{cap}}, \tag{4.25}$$

with $\bar{v} = 1.33 a_0$, a_0 the Bohr radius, and N the number of microcapillaries in our nozzle. What we briefly discussed in this section has been used in Ref. [55] to design the oven and choose the best parameters.

4.3 Measurement and Results

Let us now have a look at the results of our absorption spectroscopy measurement.

4.3.1 First Region

Before even trying to produce a collimated atomic beam with the aid of a 2D MOT, we wanted to understand our initial setup better. For this reason, we performed some absorption spectroscopy to get information about the beam. This will allow us to better notice the effect of the 2D MOT. Moreover, it will provide us additional information about what still needs to be redesigned. Let us have a look at the measurement results in the first region. We used the output of the ECDL laser to probe the atomic beam. A 15 μW beam travels perpendicularly across the atoms and is then focused onto a photodiode. The frequency of the laser is scanned and monitored with the wavemeter. We run the oven at different temperatures. The result is shown in Figure 4.6.

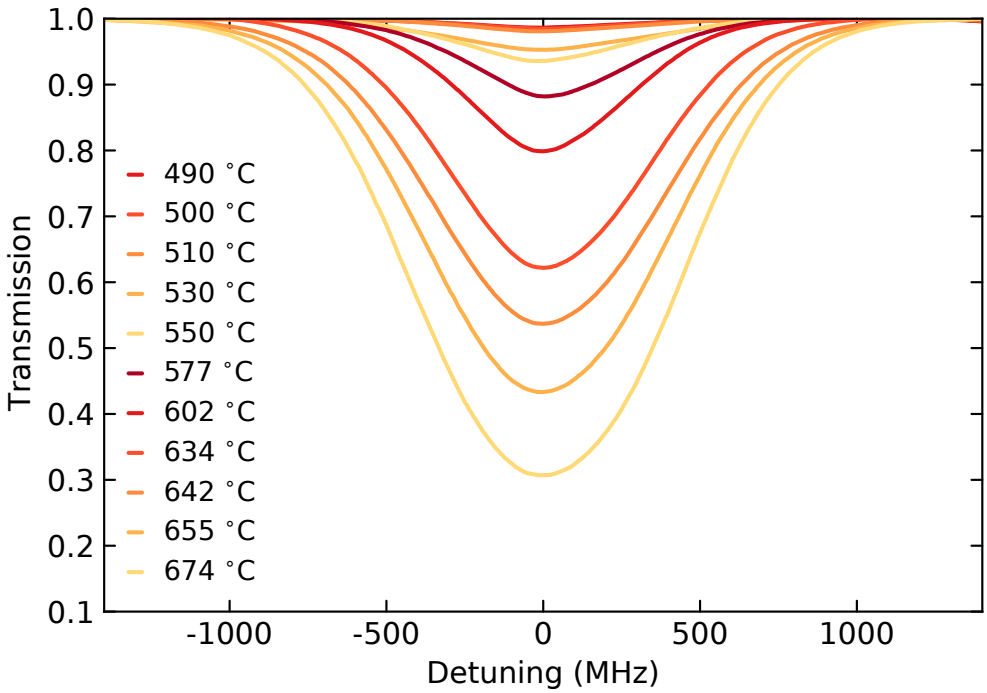

Figure 4.6 Spectra measured in the first region as a function of nozzle temperature.

The spectra are quite broad and seem to be gaussian. This is evident also when we try to fit the model to the data. The model matches the data only for very low temperatures. As temperature increases the gaussian character becomes more evident.

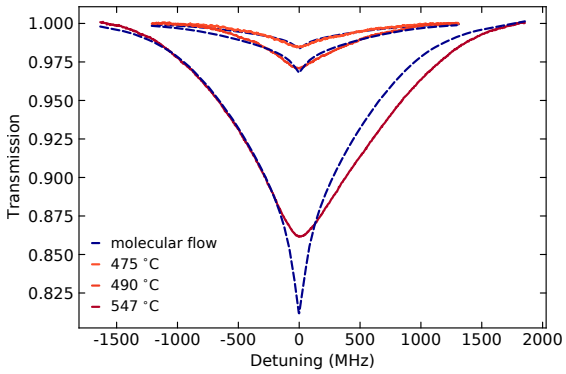

Figure 4.7 Fit attempt with the absorption profile model.

These spectra cannot be due to power broadening since no appreciable difference was noticed by reducing the laser power. The options are three, and they can be present alone or together:

- The vacuum has degraded due to a leak or due to outgassing.
- The capillaries are clogged.
- Strontium is effusing from the heat shields surrounding the crucible or from another place in the oven setup that becomes unexpectedly too hot.

Another evidence proved that something was wrong: the viewports got coated with strontium atoms. This had already happened in the past, and we thought the issue had been solved by moving the oven back from the cross. However, after running the oven for a few days at nozzle temperatures of about 700°C, we noticed a reflecting coating on each viewport. This had reduced the transmission at each viewport to about 65%, which could have also made the construction of the 2D MOT impossible or at least a lot more complicated. For this reason, we stopped and tried to get rid of the strontium.

Baking of the Viewports

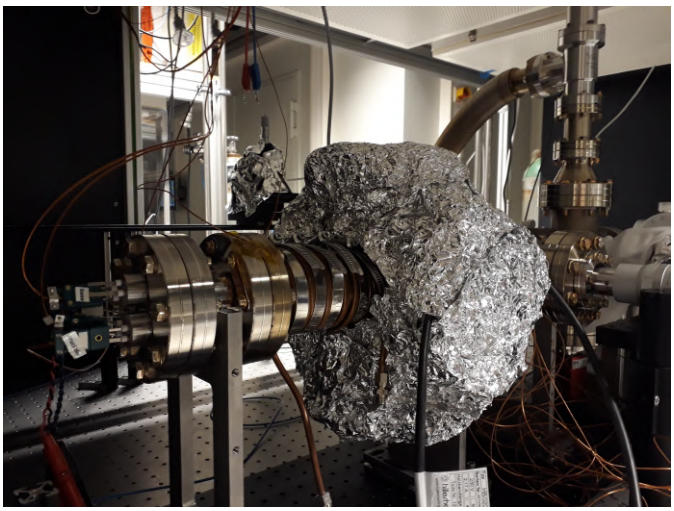

Figure 4.8 Baking of the viewports.

There was no possibility to clean the viewports by unmounting them since the exposure to air of strontium would have oxidized it, and it would have been then impossible to remove it without scratching the windows. For this reason, we applied the same procedure of Ref. [55]. We baked the viewports for one week. For this purpose, metal plates with thermocouples glued on were fixed to each viewport. These protected the viewports and allowed uniform heating. The cross was then wrapped with aluminum foil. On this, we placed the heating tape. We wanted to avoid heating the center of the cross to prevent the strontium stuck there from moving towards the viewports, which would have undermined the try or even worsened the coating. Simultaneously, the heating tape cannot lie "in the air", so some contact could not be avoided. In the end, the center

of the cross was about 60°C colder than the viewports. The setup was then wrapped again with aluminum foil, then fiberglass and aluminum foil again. We heated the viewports up to around 190°C, paying attention never to reach a temperature change of 2°C/min and not to reach 200°C, which could have broken the windows. After a week, the transmission had improved to about 82% per window, with different values depending on the viewport's region at which we were looking. We tried to bake again for about another week, but no significant improvement was noticed.

The baking procedure required having a pump connected, which allowed us to check the pressure hypothesis directly. We could reach a pressure of 1.7×10^{-7} mbar. Then we retook the data. The result is shown in Figure 4.9.

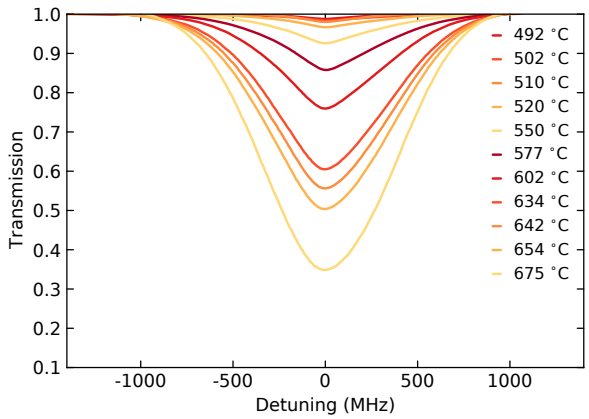

Figure 4.9 Absorption spectra taken in the first region after pumping. The distributions are narrower, but the peak height is also smaller.

The pump did not improve the situation much. The spectra became a little bit narrower, for example, about 10% at 675°C. At the same time, the peak height became smaller. The data is still incompatible with the theoretical model, so we conclude that our capillaries must be clogged, and we must also have some strontium diffusing from the heat shields. We decided to keep the setup like this since trying to clean the nozzle could have been dangerous. Another nozzle with a different aspect ratio had already been scratched in the process and became unusable. We also did not have spare capillaries to mount another one, so we decided to quickly test the effect of a molasses beam to see if there was some effect on the beam. The test showed appreciable effects, so we decided to keep the setup.

4.3.2 Second Region

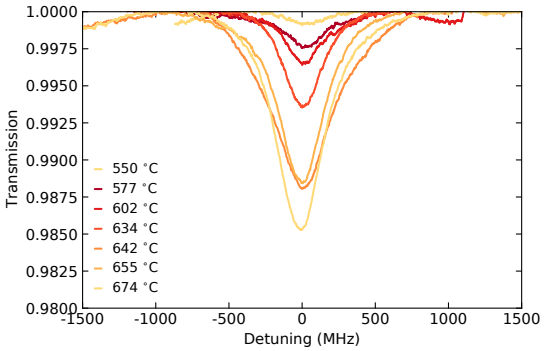

Figure 4.10 Absorption spectra measured with one passage in the second spectroscopy region.

Additional information about the atomic beam can be gathered in the second spectroscopy region. The viewports that we will use are about 42 cm away from the first region. The results confirm the strong divergence of our beam; even at 675°C, we get less than 2% absorption. This can be seen in Figure 4.10. Moreover, it becomes challenging to analyze the signal since the feature becomes really small. This data made us doubt that the setup could allow us to notice the effects of the 2D MOT. This is because it would not have been enough to notice an increased peak height, but we also wanted to be able to discern one magnetic field configuration from the other, which appeared impossible. The solution that we came up with was "multipass absorption spectroscopy". With this, we mean that the light beam is reflected on two 2" mirrors back and forth 11 times, as illustrated in Fig. 4.11.

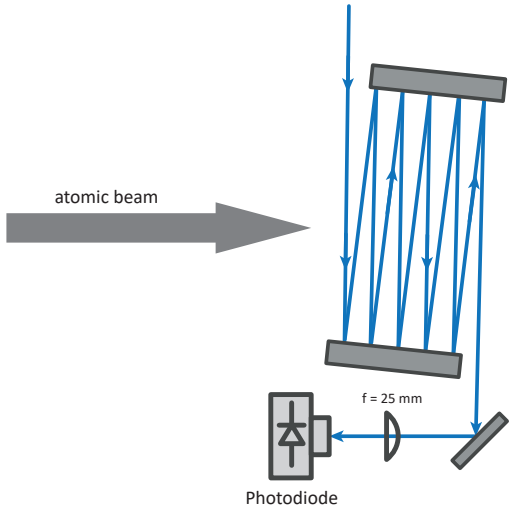

Figure 4.11 Scheme of the setup we used to enhance the second region's signal to detect small changes in the atomic distribution.

The results are shown in Figure 4.12.

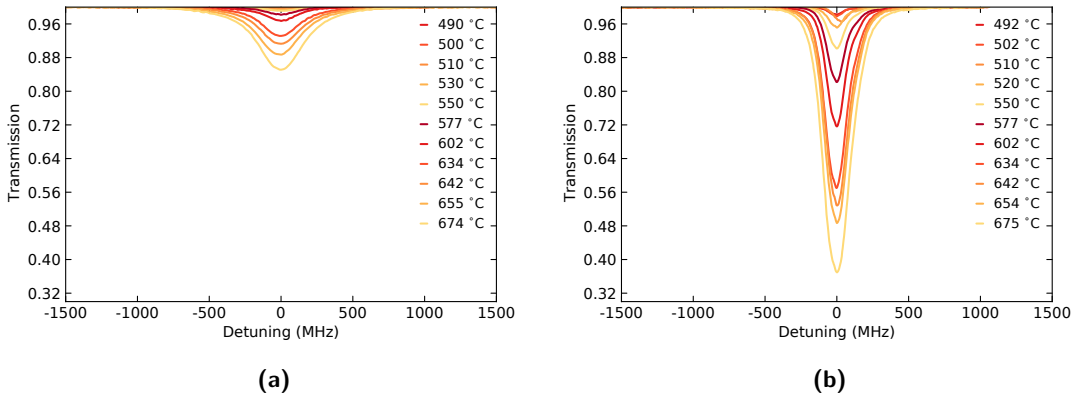

Figure 4.12 Spectra measured in the second region as a function of nozzle temperature. (a) Data taken before pumping. (b) Data taken after the pumping session.

In this case, we can really notice the effect of the pump. The peak height is much higher than before, meaning that the atoms are now colliding less with background gas and thus have a higher chance to reach the second region. Nevertheless, if we think that we are multiplying the real absorption ten times, the absorption maximum is for $T = 675°\text{C}$ around 6%. So, a tiny fraction of atoms survives till to the second cross.

With this multipass method, we will try to use the razor blade to get more information about the spatial distribution of the atomic beam.

4.3.3 Razor Blade

The razor blade has an excursion of 50 mm that allows us to cover the atomic beam. As the razor blade covers the beam, we expect the peak height to reduce and the feature to change. This would be a consequence of the velocity distribution. We would intuitively expect the high-velocity atoms to be those further away from the z-axis, so as we start to move the razor blade, we expect to block those atoms. Let us look at the result of this measurement.

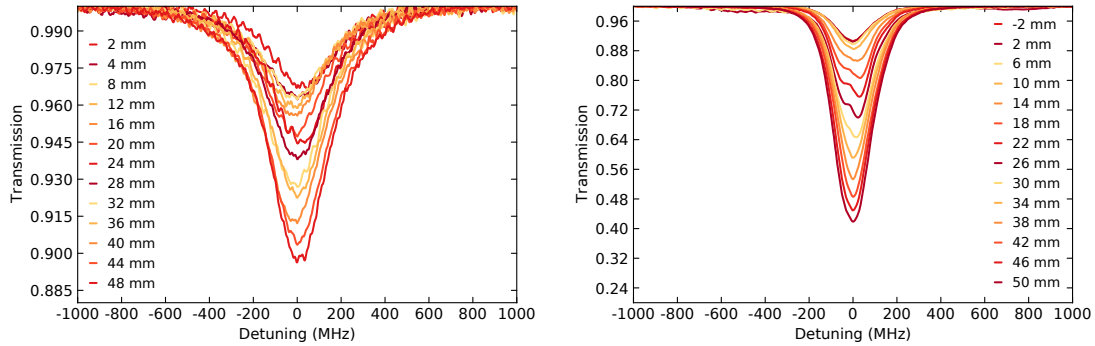

(a) **(b)**

Figure 4.13 Spectra as a function of razor blade position. Both the data sets have been taken with the multipass configuration. (a) Spectra for different razor blade positions before pumping. (b) Spectra as a function of razor blade position after pumping.

Also in this case, we notice an improvement in the measurement due to the improved vacuum. First of all, the multipass allows better discerning of the different razor blade positions; second, the vacuum improvement allows seeing the effect of Doppler shift. As the razor blade moves towards the chamber center, it covers the atomic beam. We expect to be covering high-velocity atoms with velocity parallel to the laser beam first. These atoms would have a negative detuning due to the factor $-\mathbf{k}\cdot\mathbf{v}$. This is what we see in Fig. 4.13 (b), the shift of the peak towards positive detuning and the appearance of a second peak on the left. A single peak is recovered for the closed case. This is consistent with what we expect since the razor blade does not cover the whole beam, leaving space underneath and above the razor.

We would have liked to be able to extract the number of atoms fitting the data with the models discussed in Section 4.2.2. However, the data was far away from what we expected. Even if we were not able to get quantitative information about the beam, we showed from one side what still has to be improved on the setup, and on the other side, we were able to show the ability of the spectroscopy procedure to analyze the beam. Related to this, we were able to see the effect of Doppler shift thanks to the razor blade.

We will now move to the last tool that we need before building the 2D MOT: a three-axis

translation stage to measure magnetic fields.

Chapter 5

Magnetic Fields with Permanent Magnets

We said that to build a 2D MOT, we need a spatially dependent magnetic field. This field can be produced with coils or with permanent magnets. Both setups have already been implemented in different forms in other experiments [17, 18, 65, 66]. We opted for permanent magnets for two reasons. Permanent magnets are cheaper and require less engineering. Coils require the design of mounts, consume power, and need water cooling. Additionally, switching on and off magnetic fields could perturb the system. For these reasons, we decided to use neodymium magnets. They have dimensions $10 \times 25 \times 3$ mm^3 and have already been used in other labs [67, 27]. Now that we have our magnets, we would like to measure the field they produce in all three dimensions over a large volume. With this purpose in mind, we built a three-axis translation stage to automate the process.

5.1 Magnetic Field Measurement

We already have a three-axis Fluxgate magnetometer (Sensys FGM3D/1000), which has a high sensitivity but cannot measure fields as high as those of our magnets. We looked for an alternative and, between too expensive or not enough precise probes, we found a good compromise in a chip: the Melexis Triaxis® Magnetic Node (MLX90393) controlled via the Adafruit MLX90393 Library for Arduino. This is a wide range sensor that allows 16-bits measurements in ranges from $\pm$5 mT to $\pm$50 mT in all three axes. It offers up to $\sim$ 500 Hz sample rate. It also has an user-adjustable I2C address to allow multiple sensors in the same project. In the Adafruit MLX90393 Wide-Range 3-Axis Magnetometer, it has been placed onto a breakout board, with a 3.3V power supply and level shifter. This allows the use of both 3 and 5 V microcontrollers. We are using an Adafruit Feather M0. Additionally, the board has an on-board temperature sensor. The magnetic field resolution can be programmed. For the x-, and the y-axis it can be between 3.220 and 0.161 μT/LSB, for the z-axis between 5.872 and 0.294 μT/LSB. Apart from the good performance, we could also easily mount it on a simple acrylic support or on a translation stage.

5.1.1 3-axis High Field Magnetic Measurement Stage

For our measurement to be precise, a good probe is not enough. We usually put our magnetometer on a rail and manually move it to different positions. No matter how

good the movement is done, this is still a source of error. The rail could be misaligned, the reading of the position value could be affected by parallax error, or the rail carriage could be fixed each time in a different way. We would like to avoid all these errors as far as possible.

We decided to use a three-axis translation stage, similar to the one used in Ref. [68]. The stage is constituted from three long distance translation stages by Standa (7T175-100). These have integrated driving screws for very precise and long travel translation. The pitch of the screws is 0.5 mm, and the maximum translation is 100 mm. We also used an angle bracket (2AB175) to assemble the z-axis. We then designed support plates to be able to add step motors. Before looking at the final version of the stage let us say a few words about step motors. This section is based on Refs. [69, 70].

Step Motors

We will use hybrid bipolar step motors (SparkFun Electronics ROB-10846), but what does this mean? In general, step motors are brushless DC electric motors that divide the full rotation into a number of equal steps. They are purposely built for high-holding torque, which enables to incrementally step to the next position. Their main advantage is the low price and the high reliability. They can be used in open-loop and realize different speeds. The main disadvantage is the resonance effects that they might exhibit at low speed[1]. Step motors can be divided into three categories:

- *Variable reluctance motors* In this case, the rotor is made of some soft magnetic material. The working principle is shown in Fig. 5.1 (a). When current is applied to a winding circuit in a particular pole, the tooth of the rotor is magnetically attracted to that pole. This way the motor rotates by a defined angle. As current is turned off and consequently turned on in the next pole the rotor will move again. The principle is that minimum reluctance occurs for minimum gap.

- *Permanent magnet motors* This motor has a permanent magnet for rotor, so it does not require teeth. The scheme is shown in Fig. 5.1 (b).

- *Hybrid motors* An hybrid motor combines characteristics from the previous two. They are made up of multi-toothed stator poles and a permanent magnet rotator, which enables rotations of really small angles.

The differences exist not only in the rotor, but also in the windings:

- *Unipolar* If we call each group of poles *phase*, unipolar motors have one winding with center tap for every phase. This implies that we can reverse the magnetic field without inverting the current.

[1] Driving a motor with a stepping rate near the resonant frequency can produce random motion.

- *Bipolar* In this case, there is a single winding per phase, so the current has to be reversed. This translates into more complicated circuitry. On the other hand the space is used in a better way and the motor can be made more powerful.

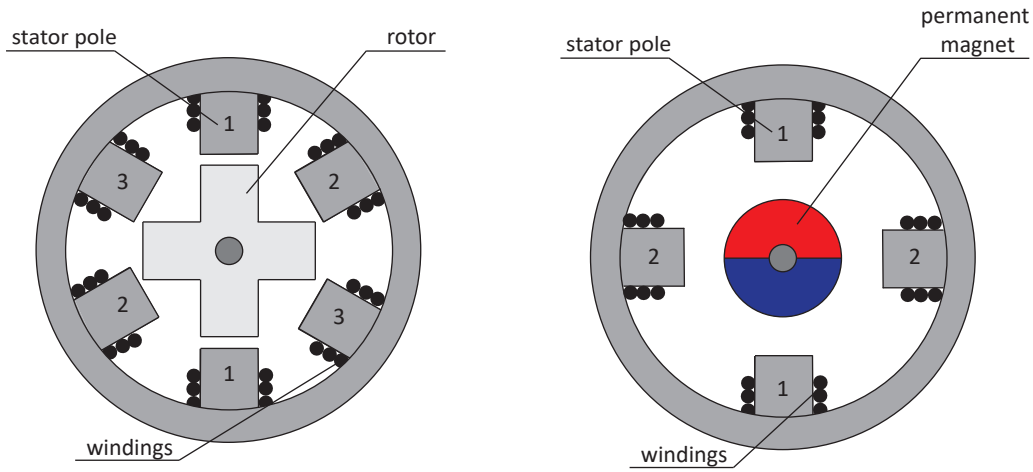

Figure 5.1 Stepper motor cross sections. (a) Variable reluctance motor. (b) Permanent magnet motor.

Last but not least there are the step modes. Operation in *full step* means that we have two phases always on. *Half step* mode is realized by overlapping drive currents. We alternate two phases on with just one on. Overlapping phases means also less torque, which may be overcome by increasing the current. *Microstepping* instead, requires a chopper drive circuit, which enables to control the currents, rather than just turn on and off a constant voltage. This allows smaller steps, which in turn produces fine resolution and a smoother rotation.

Let us say a few more words on step motors theory to be able to understand the specifications in Table 5.1. A step motor is characterized by a torque that varies with the angular position of the rotor. The shape of this curve depends on the type of motor, but we can think about the ideal sinusoidal case. We then call *holding torque* the maximum value when the maximum current is flowing through one motor winding. When no current is flowing, the torque does not become zero due to the materials' properties. This torque is called *detent torque*. If we operate in half step mode, two windings are powered, which means that we need to add the two torque curves. The two-winding holding torque will then be given by $\sqrt{2}t$, with t the single-winding holding torque. This is the value usually shown on datasheets. In case of microstepping, the torque is modified by a factor that depends on the current flowing through the different windings. Other used notations

are those of *pull-out torque* and *pull-in torque*. The first is the frictional torque that the motor can overcome on a load before the load is pulled out of step by the friction. The second is the torque that can be overcome to accelerate the load to synchronous speed.

This introduction did not take friction into account. Static friction for example, implies that a constant torque is required just to overcome it. As a consequence, less torque is available for the rotation and *dead zones* are produced. In these regions, the frictional torque balances the windings' one and the motor cannot move. The presence of these regions limits accuracy.

Parameter	Value
Phase	2 phase
Step angle	$0.9 \pm 5\%$ °/step
Voltage	3.06 V
Current	1.7 A/phase
Resistance	$1.8 \pm 10\%$ Ω/phase
Inductance	$2.8 \pm 20\%$ mH/phase
Holding Torque	48 N cm (min)
Detent Torque	2.2 N cm (max)

Table 5.1 Stepper motors specifications.

We will control our motors via the Big Easy Driver board [71], which is designed for bipolar step motors with currents up to 2A/phase. It is a chopper microstepping driver which defaults to 16 step microstepping mode. The board just needs between 8 and 35 V DC and can be controlled via an Arduino board. We used the Arduino Leonardo ETH. A python program communicating with the board via serial port has then be used to control the stage movement and the magnetic field measurement simultaneously. Additionally to the four pins to connect the 4 coils of the motor and the basic logic pins to enable the motion of the motor, it has three logical pins to select the excitation mode. Different combinations of HIGH and LOW produce different resolution: full step, half step, quarter step, eight step or sixteenth step. An additional pin allows choosing of clockwise or counterclockwise motion. Last but not least, a potentiometer allows to set the right current for every supported motor.

This brief overview taught us something important: stepper motors produce magnetic fields, whether due to currents or to the presence of permanent magnets, these fields might influence our magnetic field measurement. For this reason, we decided to place the motors away from the stage. The first version of the stage had long flexible shafts to transfer the rotation from the motors to the Standa stages. These would have allowed positioning of the motors far from the magnetic probe, and would also have required less space than fixed shafts. However, as we tested the setup, we noticed a problem. As the motor moved in a defined direction, the "fibers" of the shaft got twisted inside their tubing. When turning on and off the motors or going in the opposite direction,

this produced an hysteresis effect and prevented the translation stage to move to the desired positions or even blocked the rotation. For this reason, we opted for fixed metal rods, long enough to make the motor's field of the order of the probe error. This setup is shown in Fig. 5.2.

Figure 5.2 Three-axis translation stage with stepper motors. The three 100 mm translation stages are fixed on metal plates and driven by three stepper motors.

We now have all the tools to measure magnetic fields. We would like to measure the field given by a single magnet and get from this a value for the magnetization to be later able to design different magnetic field configurations.

5.1.2 Field Produced by a Single Magnet

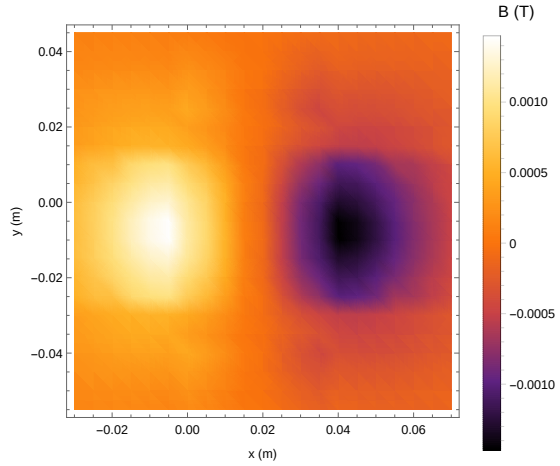

Figure 5.3 Field along of a single permanent magnet.

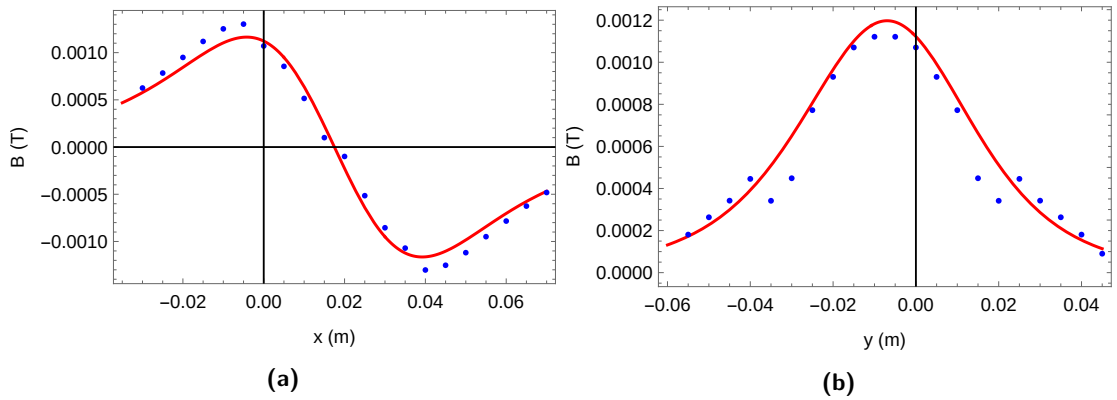

Figure 5.4 Fit results for a single magnet.

In Fig. 5.3 is shown an example of magnetic field measurement result, namely the field produced by a single magnet. From this we want to obtain a value for the magnetization. For this we used equations given in Ref. [66], adapted from Refs. [72, 73]. The fit is

shown in Fig. 5.4 for two different axes.

$$
\begin{aligned}
B_x(x,y,z) = &+ \frac{\mu_0 m_x}{4\pi} \sum_{i,j,k=0}^{1} (-1)^{i+j+k} \text{atan}\left(\frac{(y-y_j)(z-z_k)}{(x-x_i)\sqrt{(x-x_i)^2+(y-y_j)^2+(z-z_k)^2}} \right) \\
&- \frac{\mu_0 m_y}{4\pi} \sum_{i,j,k=0}^{1} (-1)^{i+j+k} \text{asinh}\left(\frac{z-z_k}{\sqrt{(x-x_i)^2+(y-y_j)^2}} \right) \\
&- \frac{\mu_0 m_z}{4\pi} \sum_{i,j,k=0}^{1} (-1)^{i+j+k} \text{asinh}\left(\frac{y-y_j}{\sqrt{(x-x_i)^2+(z-z_k)^2}} \right) \\
B_y(x,y,z) = &+ \frac{\mu_0 m_y}{4\pi} \sum_{i,j,k=0}^{1} (-1)^{i+j+k} \text{atan}\left(\frac{(x-x_i)(z-z_k)}{(y-y_j)\sqrt{(x-x_i)^2+(y-y_j)^2+(z-z_k)^2}} \right) \\
&- \frac{\mu_0 m_z}{4\pi} \sum_{i,j,k=0}^{1} (-1)^{i+j+k} \text{asinh}\left(\frac{x-x_i}{\sqrt{(y-y_j)^2+(z-z_k)^2}} \right) \\
&- \frac{\mu_0 m_x}{4\pi} \sum_{i,j,k=0}^{1} (-1)^{i+j+k} \text{asinh}\left(\frac{z-z_k}{\sqrt{(x-x_i)^2+(y-y_j)^2}} \right) \\
B_z(x,y,z) = &+ \frac{\mu_0 m_z}{4\pi} \sum_{i,j,k=0}^{1} (-1)^{i+j+k} \text{atan}\left(\frac{(x-x_i)(y-y_j)}{(z-z_k)\sqrt{(x-x_i)^2+(y-y_j)^2+(z-z_k)^2}} \right) \\
&- \frac{\mu_0 m_x}{4\pi} \sum_{i,j,k=0}^{1} (-1)^{i+j+k} \text{asinh}\left(\frac{x-x_i}{\sqrt{(x-x_i)^2+(y-y_j)^2}} \right) \\
&- \frac{\mu_0 m_y}{4\pi} \sum_{i,j,k=0}^{1} (-1)^{i+j+k} \text{asinh}\left(\frac{x-x_i}{\sqrt{(y-y_j)^2+(z-z_k)^2}} \right),
\end{aligned}
\tag{5.1}
$$

where (x_0, y_0, z_0) are the coordinates of a corner of the permanent magnet and (x_1, y_1, z_1) those of the opposite one. (m_x, m_y, m_z) is the magnetism vector $M = B_R/\mu_0$, with μ_0 the permeability of vacuum and B_R the residual magnetization. We fitted the data to get an idea of the magnetization value. This could of course be a bit different from magnet to magnet, but we just wanted to get an idea of the fields we could produce. We found a magnetization value of:

$$M = 1.13(9) \times 10^6 \text{A/m}. \tag{5.2}$$

Later we found that the usual ideal magnetic dipole equation, Eq. (5.3), could describe the field produced by the magnets well enough.

$$\mathbf{B}(\mathbf{r}) = \frac{\mu_0}{4\pi} \left[\frac{3\hat{\mathbf{r}}(\mathbf{m}\cdot\hat{\mathbf{r}}) - \mathbf{m}}{r^3} \right], \tag{5.3}$$

with $\hat{\mathbf{r}}$ the unit vector in the direction of $\mathbf{r}$ and $\mathbf{m}$ the magnetic moment; this is related to the magnetization via the volume of the magnet V:

$$\mathbf{m} = \mathbf{M}V = \frac{1}{\mu_0}\mathbf{B_r}V. \tag{5.4}$$

With this background we can now look at the shape of the 2D MOT field.

5.2 Magnetic Field Design

5.2.1 Magnetic Field for a 2D MOT

In section 2.4.2, we mentioned the shape of the required magnetic field:

$$\mathbf{B} = b\mathbf{x} - b\mathbf{y}, \tag{5.5}$$

This field can be produced by four stacks of magnets arranged as shown in Fig. 5.5. The stacks are placed at the corners of an imaginary rectangle centered in $(0, 0, 0)$ in the coordinate system given by the cooling beams and the atomic beam axis.

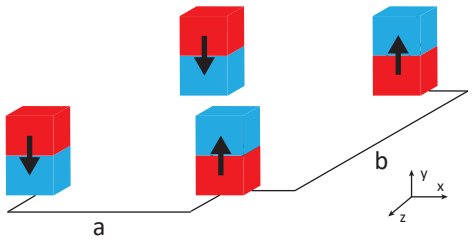

Figure 5.5 Arrangement of four stacks of permanent magnets to the corners of an imaginary rectangle of size $a \times b$ centered in $(0, 0, 0)$. The cartesian axes x, y represent the laser beam's plane.

We wanted to get an idea of the dimensions we need to have to get a uniform gradient in the 2D MOT volume, with no sign flips or large gradients along the z-axis. Therefore we used Eq. (5.3) to simulate the field. First we checked the field derivative in the cross volume, which is approximated by a cube of side 60 mm. We found it to be constant for every possible magnet configuration allowed by the dimensions of our chamber so we moved on. Then we looked at the zero field line and at how the field profile changes along the z-axis. Ideally we would like to have a field that, for fixed values of x and y, looks flat along the z-axis.

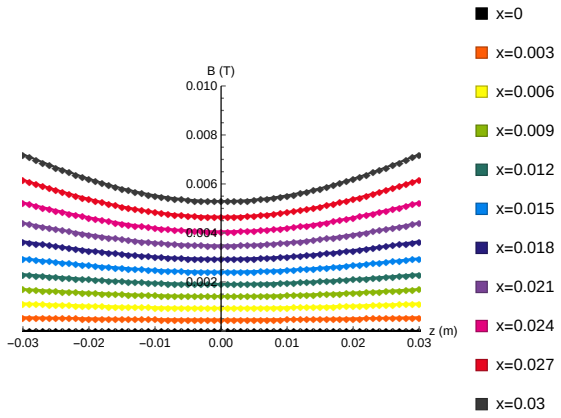

Figure 5.6 Simulation of the field along the z-axis, with magnet separation 175 mm along x, 115 mm along z, and 5 magnets per stack.

Although the field is not flat for the whole cross volume, it stays flat inside the volume that our laser beams will have, which is about 20×10 mm^2. This is true quite in general for different magnet configurations, with different distances along x and z, so we think the field shape along z would not be a problem for us.

The field in the plane given by the cooling beams should look like what shown in Fig. 5.7. The cooling beams will have to lie on the diagonals.

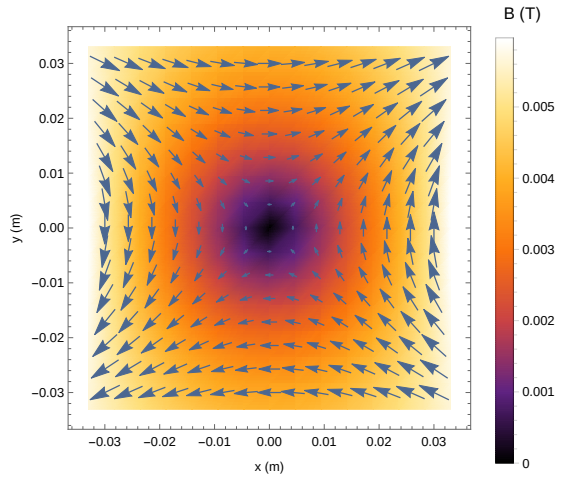

Figure 5.7 Simulation of the field for $z = 0$, with magnet separation 175 mm along x, 115 mm along z, and 5 magnets per stack.

Fig. 5.8 shows how the field should look like on the xz plane. We can clearly see the zero field line.

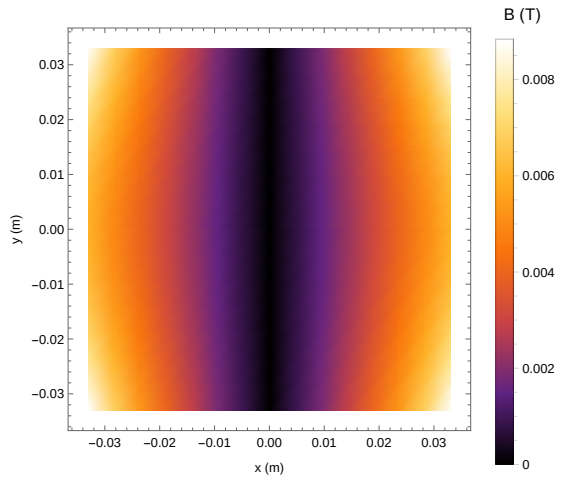

Figure 5.8 Simulation of the field for $y = 0$, with magnet separation 175 mm along x, 115 mm along z, and 5 magnets per stack.

This has all been done with magnets on the horizontal plane. In practice we will have to mount the magnets at 45°. This will be done with some simple acrylic mounts that will also allow to try different magnetic field configurations.

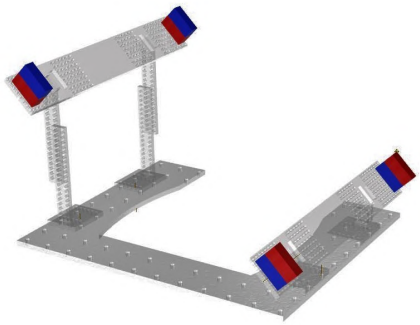

Figure 5.9 Render of the permanent magnets mounting stage.

Now that we have our mounting stage, we can look at an example of measured magnetic

field.

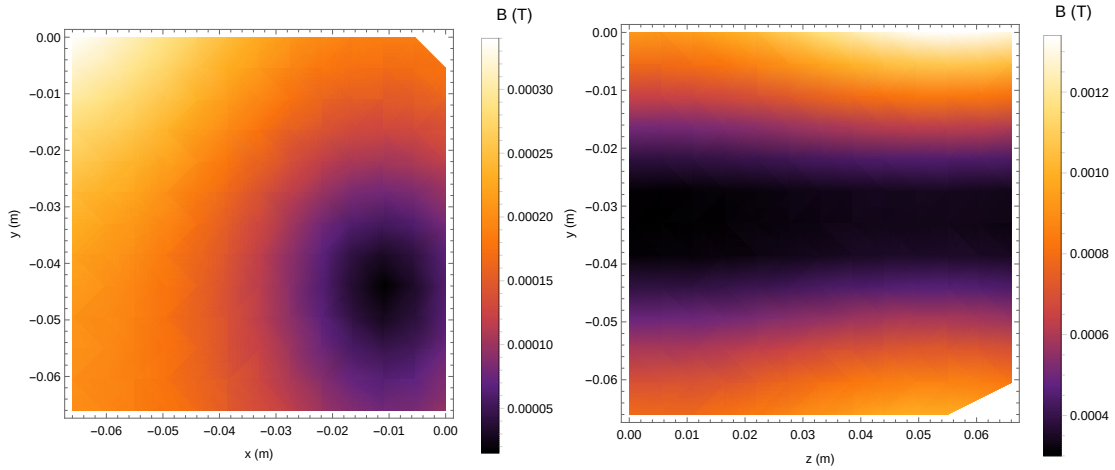

(a) **(b)**

Figure 5.10 Magnetic field measurement 175×115 mm^2. (a) Cooling beams plane. (b) Plane along the atomic beam.

In literature there are already 2D MOT setups for strontium but they are different from what we will build due to the oven mounting direction. This means that we will have to try different configurations to find the best gradient.

Chapter 6

2D MOT

We now have all the tools to build our 2D MOT. We have an idea of how to place the permanent magnets to produce a quadrupole field, and have a laser that outputs enough power to be able to collimate the atomic beam even in presence of low viewport transmission. In this chapter we will first describe the laser setup and then move to the results.

6.1 Setup and Measurement Procedure

In principle our laser setup could be made up of just two retroreflected beams. However, if the OD is too high, the atoms absorb too much light and retroreflecting could produce a power imbalance between the molasses beams. In principle we could have overcome this issue by operating at low OD and reducing a little bit the beam size, adapting the waist to maintain a constant saturation parameter. But given the condition of our viewports, we thought it would have been better to use four separate beams. This increased the system size, but also allowed an easier tuning of the power of each beam. In practice we have four arms with the same optics to get the same beam size. An example of an arm is shown in Fig. 6.1. With the telescope we obtain a beam of dimensions 2.5×1 cm^2. We chose to make the beams elliptical since the forward velocity of the atoms is much higher than the transverse one, if the beams were too small on that direction, the atoms could not have enough time to scatter light and be slowed down.

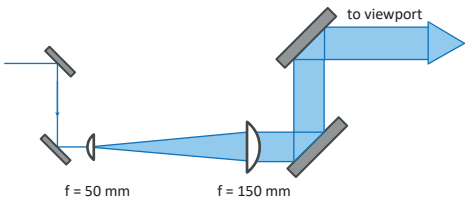

Figure 6.1 Example of the optics setup of one cooling arm.

All the arms look the same but are built on different breadboards and are quite far apart so the actual beam size is a bit different for every arm. This happens since the beam is a little bit divergent over such long paths. Still, we can use half-wave plates to tune the power of each beam and balance the forces. All the optics we need to tune the power and set the polarization of the beams lie on the "laser table". The whole setup is shown in Fig. 6.2.

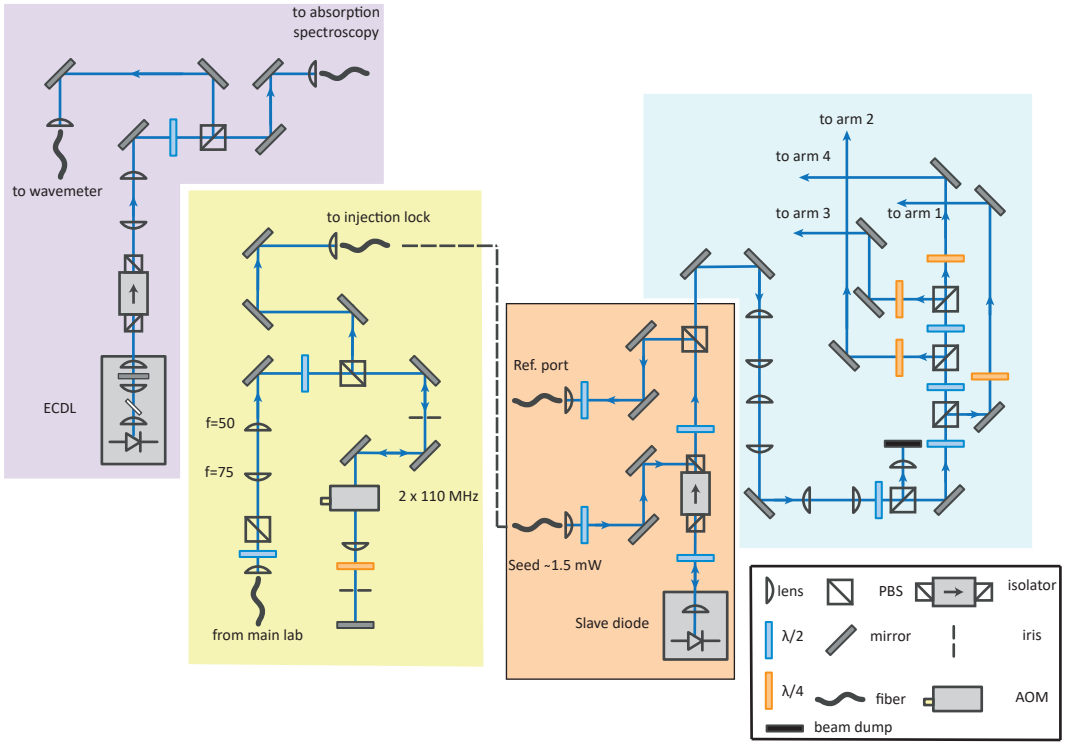

Figure 6.2 Laser table optics.

On the laser table lies our ECDL laser for absorption spectroscopy, the injection lock case and all the optics we need to produce four cooling beams. As said in section 2.4.2, the cooling beams have to be red-detuned. We choose to lock our slave laser with light referenced to the resonance transition of ^{88}Sr thanks to a spectroscopy cell that is being used in the main experiment. We have then an optical fiber that brings this light from one lab to the other. When we couple the light, this has already been shifted -234 MHz for other purposes, so we need to shift it back to detunings of the order of Γ. To do this we use an acusto-optical modulator (AOM) in doublepass configuration. The AOM has a central frequency of 110 MHz.

Double passing The doublepass AOM configuration not only can be used to double the frequency shift, but is also more stable, since it can compensate for beam deflections

[74]. For double passing we need two mirrors to align the beam to the AOM, which gives a first shift. The beam gets then inside the cateye configuration where an iris selects the right diffraction mode. The beam is then reflected back to the AOM, where it gets shifted again. The quarter-wave plate is used to rotate the polarization such that the beam exits the PBS on the other side. We get a 51% efficiency.

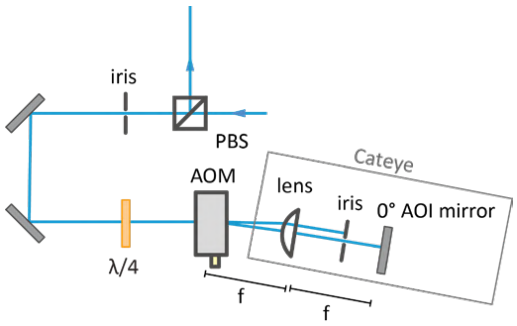

Figure 6.3 Double pass AOM setup.

In general we will work with 20 MHz of detuning. After this, the light is coupled into a fiber and used as seed for the slave laser. Finally the slave laser is used to build the four beams. We do some beam shaping to bring our beam to an elliptical shape, with the horizontal waist about two times the vertical one. The size is at this point limited by the PBS size. We have then the half-wave plates to split the beam and the quarter-wave plates to go to circular polarization.

Before looking at the results let us briefly mention how the setup in the main experiment looks like. The blue laser system of the main experiment consists of an ECDL master laser, which is locked to the ^{88}Sr $^1S_0 \rightarrow ^1P_1$ transition in a spectroscopy cell and then seeds some injection lock modules. Each of them can output ~ 100 mW of power. We want to be able to achieve a MOT with all the isotopes, so we use a broadband 350 MHz AOM (shown in red in Fig. 6.4) in doublepass configuration. Before that, a single pass AOM subtracts -350 MHz, so we end up with an offset of 234-504 MHz. The positive detuned frequency is then sent to the spectroscopy cell and the detuning of the broadband AOM set so that the output laser is always -234 MHz detuned from each isotope transition. This is the light that we also use. Details on the other parts of the setup can be found in Ref. [29].

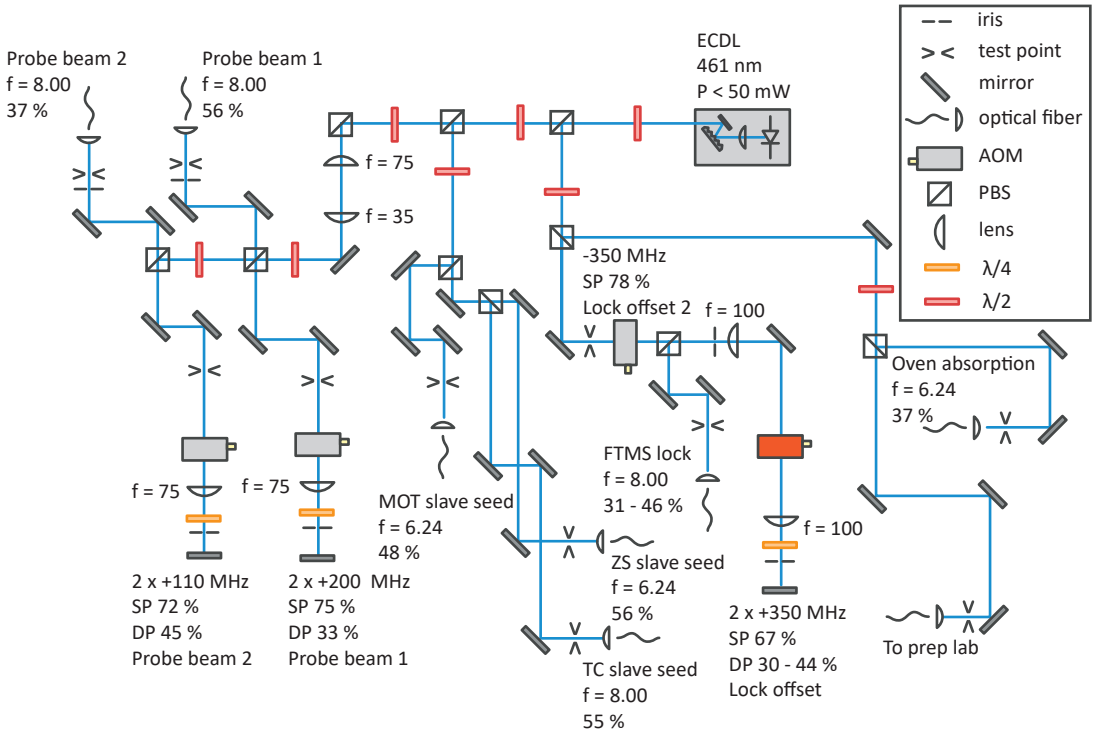

Figure 6.4 Main experiment blue laser system.

We can now move to the measurement of the 2D MOT's performance.

6.2 Results

First of all we wanted to know the effect of 1D molasses cooling for different oven temperatures and different molasses power. As the temperature changes, the number of atoms and the velocity distribution also changes. In one word, as the temperature changes, the OD changes. If the OD is too high, it might happen that the cooling light gets absorbed before it reaches the "right" atoms and we could see no effect on the absorption signal in the second region. On the other hand, different values of power means different saturation parameter s_0, since the beam size remains the same. Let us have a look at the results.

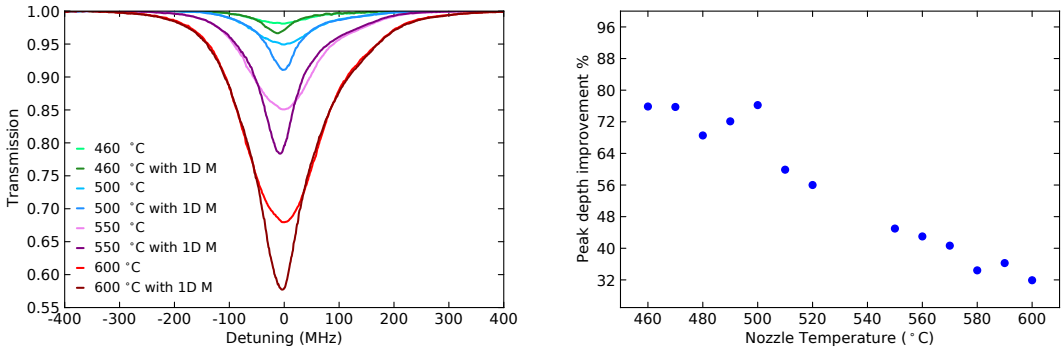

(a) **(b)**

Figure 6.5 1D molasses cooling as a function of nozzle temperature. (a) Absorption spectra with and without the molasses beams taken in the second region using multipass absorption spectroscopy. (b) Percentage increase of the number of slow atoms as a function of temperature.

Fig. 6.5 (b) shows the increase of the number of slow atoms in function of temperature. When we say the number of slow atoms, we mean that we take the peak height of the absorption spectrum and look at how much this changed compared to the bare atomic beam case. As expected, as the OD increases, the efficiency of the molasses cooling decreases. The maximum increase is $\sim 76\%$ at $460°$C, the minimum $\sim 32\%$ at $600°$C. For every data point we used about 85 mW per beam. The following figure shows how the efficiency of the molasses changes as a function of power for two different temperatures.

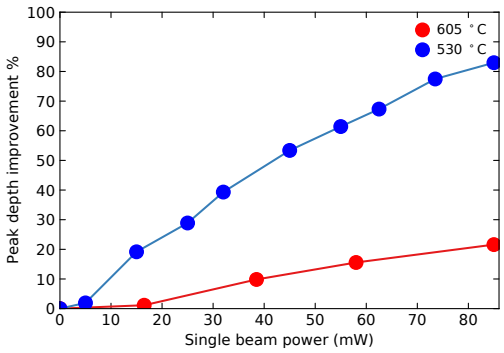

Figure 6.6 The graphs shows the increase of the number of slow atoms as a function of the single beam power. At lower temperature the differences are larger. At higher temperature the light probably gets absorbed too soon, so increasing the power leads to an improvement but not to a dramatic one. The maximum increment at $530°$C is bigger than what we saw before, but the data has been taken on a different day than Fig. 6.5 (b), so the velocity distribution of the atoms or the atom number could have changed.

A last check of the effect of a 1D molasses configuration is the atom number change as a function of the razor blade position. An actual atom number cannot be extracted since the model does not match the data, so we will plot just the integral of the logarithm of the transmission, which is proportional to the atom number.

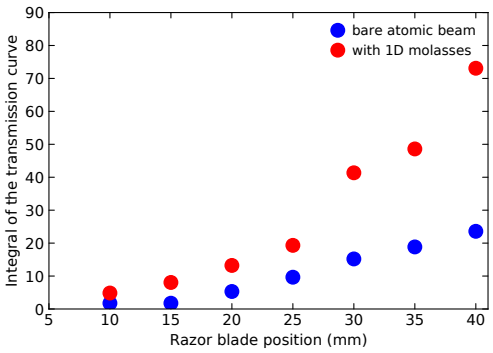

Figure 6.7 "Atom number" as a function of the razor blade position. The razor blade is completely open at 50 mm. The data was taken at 550°C and 85 mW.

We then moved to the 2D molasses cooling and checked the consistency. We would expect a factor of 2 increase with respect to the 1D case. At this point the seed power available decreased since it was needed in the main experiment so we are going to compare the results for lower beam power. We should still be able to make predictions of what we would get with all the power available.

To be able to make some prediction on the effect of 2D molasses cooling, we measured the effect of each beam separately, for $T = 530$°C and the highest power available. The absorption peak height increase is shown in Table 6.1.

Beam	Increment
Left	62.7%
Right	59.92%
Top	51.51%
Bottom	58.47%

Table 6.1 Comparison of the cooling performance of the four different beams. Left and right indicate the viewports as seen from the oven.

Three beams out of four produced comparable results, the top one is less efficient, but we are confident that with a more careful alignment it will give comparable results. Unless the discrepancy is due to a different coating of the viewport. Still we think that this result is enough to deduce the effect of four beams at full power. We expect to obtain a peak height increase of about 160% increase for low temperatures and about 60% for

higher temperatures, compare Fig. 6.5.

Finally, we tried to see the effect of the magnetic field. We tried different configurations without being able to see a contribution. Even when an effect might be present, we cannot really claim that the effect is due to the field and not just due to a really small temperature increase. We believe that the magnetic field contribution should be investigated further, trying also different detunings, which, with our low seed power, would have required realigning the AOM.

We also tried to see if we could deflect the atomic beam by tilting the magnets. We tilted the magnets about $5°$ and looked at the absorption spectra in function of the razor blade position.

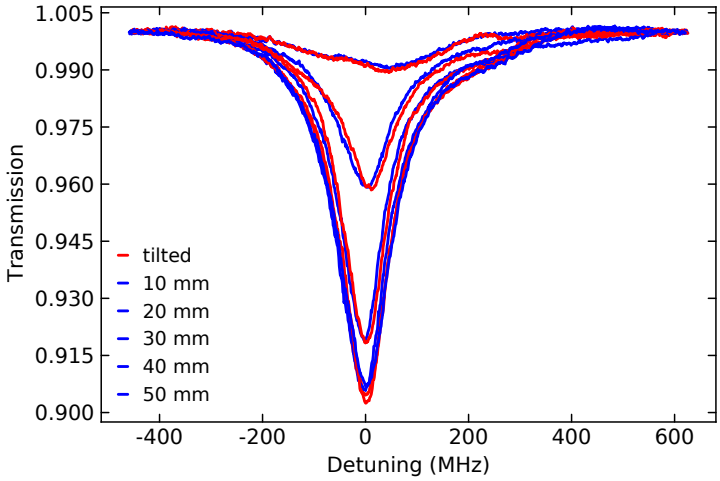

Figure 6.8 Attempt of deflection of the atomic beam.

We see that one magnetic field configuration delivers more atoms than the other. We are not completely sure if this is really just due to the magnets and not due to some other effect. Also, the effect is so tiny that the result might also be biased by our data analysis. When analyzing the data, we fit a line to get rid of the slope and obtain transmission equal to 1 for no atoms. The fit is quite sensitive to the data points that we fit on the two sides of the dip, so we might just be normalizing differently.

In this chapter, we discussed a 2D MOT setup and demonstrated the cooling effect of 2D molasses. The magnetic field contribution, which should focus the atomic beam, still needs to be studied. Still, we can claim a minimum increase in the slow atom number between 160% and 60%, depending on the temperature.

Chapter 7

Conclusion and Outlook

The aim of this thesis was the construction of a 2D MOT for strontium using permanent magnets. The purpose of this device is to produce a high-flux beam of slow atoms by collimating the atomic beam effusing from an oven. In Chapter 4, we reported the result of absorption spectroscopy performed in the two spectroscopy regions of our vacuum chamber. We probed the atomic beam for different temperatures to quantify the flux. This was not possible due to clogging of the nozzle, which produced a velocity distribution that did not match the model discussed in Chapter 4. Nevertheless, the measurement allowed gathering useful information for the design of the next generation of the strontium oven. We showed the importance of a large temperature gradient between nozzle and crucible and demonstrated the importance of reducing the flange temperature. Regarding this we think that the implementation of in-vacuum water cooling should be a priority. This could reduce the temperature of the flange, which is of foremost importance if we aim to use the oven in the main setup. Moreover, it could also solve the problem given by the heat shields, from which atoms are now effusing in a thermal way. Additionally, particular attention should be put in increasing the thermal contact between the crucible bottom and the baseplate. We showed the effectiveness of our spectroscopy setup to characterize the atomic velocity distribution. In particular, the use of our multipass absorption spectroscopy allowed seeing the effect of Doppler shift, and background gas collisions on the atoms in the forward direction.

In Chapter 5 we reported the construction of a three-axis translation stage for magnetic field measurement. The stage allows measuring high magnetic fields in three dimensions and a large volume. The use of stepper motors enhances the measurement speed and reliability and automates the data taking. With this stage we measured the value of the magnetization of our permanent magnets, which was used to design the 2D MOT magnetic field, and checked our predictions.

Finally, in Chapter 6, we investigated the effect of the 2D MOT on the atomic beam. We were able to show the collimating effect of the 2D molasses cooling by looking at the increased peak height in the absorption signal. The study of this effect for different nozzle temperatures and different cooling powers has shown results consistent with our predictions. At high temperatures the optical depth is so high that, even for the maximum available power, the increase of the number of slow atoms was just about 60%. At lower temperatures, we expect this percentage to reach 200%. We find that we can use the

oven at lower temperatures to obtain slow atoms, which increases the oven operation time dramatically.

Although we can clearly collimate the atomic beam with the 2D MOT, we have not yet observed a clear signal of steering. We believe, however, that a careful optimization of detuning, laser power, and magnetic field gradient will enable this in the near future.

In the course of this thesis we also built a 448 nm laser for our Zeeman slower. We plan to use it to intercept the atoms before they decay into the triplet state. The spectrum of the laser is suitable for addressing of the 5s4d $^1D_2$ to 5s8p $^1P_1$ and narrow enough to avoid the excitation of other transitions. Preliminary tests have shown an increase of the number of atoms loaded into the blue MOT. Due to time constraints, we could not verify the stability of the system, but we believe that a better alignment of the beam and a careful tuning of the temperature will produce a considerable increase in the atom number.

In conclusion, we believe that with a little more effort in finding the optimal magnetic field and the implementation of the Zeeman repump beam will help to enhance the efficiency of the main experiment's cycle.

References

[1] Greiner, M., O. Mandel, T. Esslinger, T. W. Hänsch, and I. Bloch. *Quantum phase transition from a superfluid to a Mott insulator in a gas of ultracold atoms*, Nature **415**., 39 (2002). DOI: 10.1038/415039a.

[2] Köhl, M., H. Moritz, T. Stöferle, K. Günter, and T. Esslinger. *Fermionic Atoms in a Three Dimensional Optical Lattice: Observing Fermi Surfaces, Dynamics, and Interactions*, Phys. Rev. Lett. **94**, 080403 (2005). DOI: 10.1103/PhysRevLett.94.080403.

[3] Jotzu, G., M. Messer, R. Desbuquois, M. Lebrat, T. Uehlinger, D. Greif, and T. Esslinger. *Experimental realization of the topological Haldane model with ultracold fermions*, Nature **515**., 237–240 (2014). DOI: 10.1038/nature13915.

[4] Schauß, P., M. Cheneau, M. Endres, T. Fukuhara, S. Hild, A. Omran, T. Pohl, C. Gross, S. Kuhr, and I. Bloch. *Observation of spatially ordered structures in a two-dimensional Rydberg gas*, Nature **491**., 87 (2012). DOI: 10.1038/nature11596.

[5] Lahaye, T., C. Menotti, L. Santos, M. Lewenstein, and T. Pfau. *The physics of dipolar bosonic quantum gases*, Reports on Progress in Physics **72**., 126401 (2009). DOI: 10.1088/0034-4885/72/12/126401.

[6] Ludlow, A. D., M. M. Boyd, T. Zelevinsky, S. M. Foreman, S. Blatt, M. Notcutt, T. Ido, and J. Ye. *Systematic Study of the* ^{87}Sr *Clock Transition in an Optical Lattice*, Phys. Rev. Lett. **96**, 033003 (2006). DOI: 10.1103/PhysRevLett.96.033003.

[7] Bakr, W. S., J. I. Gillen, A. Peng, S. Fölling, and M. Greiner. *A quantum gas microscope for detecting single atoms in a Hubbard-regime optical lattice*, Nature **462**., 74 (2009). DOI: 10.1038/nature08482.

[8] Cheuk, L. W., M. A. Nichols, M. Okan, T. Gersdorf, V. V. Ramasesh, W. S. Bakr, T. Lompe, and M. W. Zwierlein. *Quantum-Gas Microscope for Fermionic Atoms*, Phys. Rev. Lett. **114**, 193001 (2015). DOI: 10.1103/PhysRevLett.114.193001.

[9] Parsons, M. F., F. Huber, A. Mazurenko, C. S. Chiu, W. Setiawan, K. Wooley-Brown, S. Blatt, and M. Greiner. *Site-Resolved Imaging of Fermionic* ^{6}Li *in an Optical Lattice*, Phys. Rev. Lett. **114**, 213002 (2015). DOI: 10.1103/PhysRevLett.114.213002.

[10] González-Tudela, A., C. S. Muñoz, and J. I. Cirac. *Engineering and Harnessing Giant Atoms in High-Dimensional Baths: A Proposal for Implementation with Cold Atoms*, Phys. Rev. Lett. **122**, 203603 (2019). DOI: 10.1103/PhysRevLett.122.203603.

[11] Krinner, L., M. Stewart, A. Pazmiño, J. Kwon, and D. Schneble. *Spontaneous emission of matter waves from a tunable open quantum system*, Nature **559**., 589 (2018). DOI: 10.1038/s41586-018-0348-z.

[12] Ludlow, A. D., M. M. Boyd, J. Ye, E. Peik, and P. O. Schmidt. *Optical atomic clocks*, Rev. Mod. Phys. **87**, 637 (2015). DOI: 10.1103/RevModPhys.87.637.

[13] Cazalilla, M. A. and A. M. Rey. *Ultracold Fermi gases with emergent SU(N) symmetry*, Reports on Progress in Physics **77**., 124401 (2014). DOI: 10.1088/0034-4885/77/12/124401.

[14] Kaubruegger, R., P. Silvi, C. Kokail, R. van Bijnen, A. M. Rey, J. Ye, A. M. Kaufman, and P. Zoller. *Variational Spin-Squeezing Algorithms on Programmable Quantum Sensors*, Phys. Rev. Lett. **123**, 260505 (2019). DOI: 10.1103/PhysRevLett.123.260505.

[15] Senaratne, R., S. V. Rajagopal, Z. A. Geiger, K. M. Fujiwara, V. Lebedev, and D. M. Weld. *Effusive atomic oven nozzle design using an aligned microcapillary array*, Review of Scientific Instruments **86**., 023105 (2015). DOI: 10.1063/1.4907401.

[16] Schioppo, M., N. Poli, M. Prevedelli, S. Falke, C. Lisdat, U. Sterr, and G. M. Tino. *A compact and efficient strontium oven for laser-cooling experiments*, Review of Scientific Instruments **83**., 103101 (2012). DOI: 10.1063/1.4756936.

[17] Nosske, I., L. Couturier, F. Hu, C. Tan, C. Qiao, J. Blume, Y. H. Jiang, P. Chen, and M. Weidemüller. *Two-dimensional magneto-optical trap as a source for cold strontium atoms*, Phys. Rev. A **96**, 053415 (2017). DOI: 10.1103/PhysRevA.96.053415.

[18] Barbiero, M., M. G. Tarallo, D. Calonico, F. Levi, G. Lamporesi, and G. Ferrari. *Sideband-Enhanced Cold Atomic Source for Optical Clocks*, Phys. Rev. Applied **13**, 014013 (2020). DOI: 10.1103/PhysRevApplied.13.014013.

[19] Dieckmann, K., R. J. C. Spreeuw, M. Weidemüller, and J. T. M. Walraven. *Two-dimensional magneto-optical trap as a source of slow atoms*, Phys. Rev. A **58**, 3891 (1998). DOI: 10.1103/PhysRevA.58.3891.

[20] Schoser, J., A. Batär, R. Löw, V. Schweikhard, A. Grabowski, Y. B. Ovchinnikov, and T. Pfau. *Intense source of cold Rb atoms from a pure two-dimensional magneto-optical trap*, Phys. Rev. A **66**, 023410 (2002). DOI: 10.1103/PhysRevA.66.023410.

[21] Catani, J., P. Maioli, L. De Sarlo, F. Minardi, and M. Inguscio. *Intense slow beams of bosonic potassium isotopes*, Phys. Rev. A **73**, 033415 (2006). DOI: 10.1103/PhysRevA.73.033415.

[22] Ramirez-Serrano, J., N. Yu, J. M. Kohel, J. R. Kellogg, and L. Maleki. *Multistage two-dimensional magneto-optical trap as a compact cold atom beam source*, Opt. Lett. **31**., 682 (2006). DOI: 10.1364/OL.31.000682.

[23] Weyers, S., E. Aucouturier, C. Valentin, and N. Dimarcq. *A continuous beam of cold cesium atoms extracted from a two-dimensional magneto-optical trap*, Optics Communications **143**., 30 (1997). DOI: https://doi.org/10.1016/S0030-4018(97)00312-X.

[24] Berthoud, P., A. Joyet, G. Dudle, N. Sagna, and P. Thomann. *A continuous beam of slow, cold cesium atoms magnetically extracted from a 2D magneto-optical trap*, Europhysics Letters (EPL) **41**., 141 (1998). DOI: 10.1209/epl/i1998-00122-9.

[25] Riis, E., D. S. Weiss, K. A. Moler, and S. Chu. *Atom funnel for the production of a slow, high-density atomic beam*, Phys. Rev. Lett. **64**, 1658 (1990). DOI: 10.1103/PhysRevLett.64.1658.

[26] Lamporesi, G., S. Donadello, S. Serafini, and G. Ferrari. *Compact high-flux source of cold sodium atoms*, Review of Scientific Instruments **84**., 063102 (2013). DOI: 10.1063/1.4808375.

[27] Tiecke, T. G., S. D. Gensemer, A. Ludewig, and J. T. M. Walraven. *High-flux two-dimensional magneto-optical-trap source for cold lithium atoms*, Phys. Rev. A **80**, 013409 (2009). DOI: 10.1103/PhysRevA.80.013409.

[28] Metcalf, H. J. and P. van der Straten. *Laser Cooling and Trapping*. Springer-Verlag New York, 1999. ISBN: 978-1-4612-1470-0.

[29] Heinz, A. "Ultracold Strontium in State-Dependent Optical Lattices." PhD Thesis. Ludwig-Maximilians-Universität München, 2020. URL: https://ultracold.sr/publications/thesis_andre_heinz.pdf.

[30] Heinz, A., A. J. Park, N. Šantić, J. Trautmann, S. G. Porsev, M. S. Safronova, I. Bloch, and S. Blatt. *State-Dependent Optical Lattices for the Strontium Optical Qubit*, Phys. Rev. Lett. **124**, 203201 (2020). DOI: 10.1103/PhysRevLett.124.203201.

[31] Cooper, A., J. P. Covey, I. S. Madjarov, S. G. Porsev, M. S. Safronova, and M. Endres. *Alkaline-Earth Atoms in Optical Tweezers*, Phys. Rev. X **8**, 041055 (2018). DOI: 10.1103/PhysRevX.8.041055.

[32] Xu, X., T. H. Loftus, J. L. Hall, A. Gallagher, and J. Ye. *Cooling and trapping of atomic strontium*, J. Opt. Soc. Am. B **20**, 968 (2003). DOI: 10.1364/JOSAB.20.000968.

[33] Nicholson, T. L. *et al. Systematic evaluation of an atomic clock at* 2×10^{-18} *total uncertainty*, Nature Communications **6**., 6896 (2015). DOI: 10.1038/ncomms7896.

[34] Muniz, J. A., D. J. Young, J. R. K. Cline, and J. K. Thompson. *Cavity-QED determination of the natural linewidth of the* ^{87}*Sr millihertz clock transition with* 30μ*Hz resolution*, arXiv: 2007.07855 (2020).

[35] Nosske, I., L. Couturier, F. Hu, C. Tan, C. Qiao, J. Blume, Y. H. Jiang, P. Chen, and M. Weidemüller. *Two-dimensional magneto-optical trap as a source for cold strontium atoms*, Phys. Rev. A **96**, 053415 (2017). DOI: 10.1103/PhysRevA.96.053415.

[36] Boyd, M. M., T. Zelevinsky, A. D. Ludlow, S. Blatt, T. Zanon-Willette, S. M. Foreman, and J. Ye. *Nuclear spin effects in optical lattice clocks*, Phys. Rev. A **76**, 022510 (2007). DOI: 10.1103/PhysRevA.76.022510.

[37] Derevianko, A. *Feasibility of Cooling and Trapping Metastable Alkaline-Earth Atoms*, Phys. Rev. Lett. **87**, 023002 (2001). DOI: 10.1103/PhysRevLett.87.023002.

[38] Yasuda, M. and H. Katori. *Lifetime Measurement of the* $^3P_2$ *Metastable State of Strontium Atoms*, Phys. Rev. Lett. **92**, 153004 (2004). DOI: 10.1103/PhysRevLett.92.153004.

[39] Boyd, M. M. "High Precision Spectroscopy of Strontium in an Optical Lattice: Towards a New Standard for Frequency and Time." PhD Thesis. University of Colorado, 2007. URL: https://jila.colorado.edu/sites/default/files/2019-05/boyd_thesis.pdf.

[40] Prodan, J. V. and W. D. Phillips. *Chirping the light—fantastic? Recent NBS atom cooling experiments*, Progress in Quantum Electronics **8**., 231 (1984). DOI: 10.1016/0079-6727(84)90019-3.

[41] Ertmer, W., R. Blatt, J. L. Hall, and M. Zhu. *Laser Manipulation of Atomic Beam Velocities: Demonstration of Stopped Atoms and Velocity Reversal*, Phys. Rev. Lett. **54**, 996 (1985). DOI: 10.1103/PhysRevLett.54.996.

[42] Watts, R. N. and C. E. Wieman. *Manipulating atomic velocities using diode lasers*, Opt. Lett. **11**., 291 (1986). DOI: 10.1364/OL.11.000291.

[43] Phillips, W. D. and H. Metcalf. *Laser Deceleration of an Atomic Beam*, Phys. Rev. Lett. **48**, 596 (1982). DOI: 10.1103/PhysRevLett.48.596.

[44] Bagnato, V. S., G. P. Lafyatis, A. G. Martin, E. L. Raab, R. N. Ahmad-Bitar, and D. E. Pritchard. *Continuous Stopping and Trapping of Neutral Atoms*, Phys. Rev. Lett. **58**, 2194 (1987). DOI: 10.1103/PhysRevLett.58.2194.

[45] Inguscio, M. and L. Fallani. *Atomic Physics: Precise Measurements & Ultracold Matter*. Oxford University Press, 2015. ISBN: 978-0-19-852584-4.

[46] Ashkin, A. and J. P. Gordon. *Stability of radiation-pressure particle traps: an optical Earnshaw theorem*, Opt. Lett. **8**, 511 (1983). DOI: 10.1364/OL.8.000511.

[47] Courtillot, I., A. Quessada, R. P. Kovacich, J.-J. Zondy, A. Landragin, A. Clairon, and P. Lemonde. *Efficient cooling and trapping of strontium atoms*, Opt. Lett. **28**, 468 (2003). DOI: 10.1364/OL.28.000468.

[48] Saleh, B. E. A. and M. C. Teich. *Fundamentals of Photonics*. John Wiley & Sons, Ltd, 1991. ISBN: 9780471213741.

[49] Chow, W. W. and S. W. Koch. *Semiconductor-Laser Fundamentals*. Springer, Berlin, Heidelberg, 1999. ISBN: 978-3-662-03880-2.

[50] Nakamura, S., S. Pearton, and G. Fasol. *The Blue Laser Diode. The Complete Story*. 2nd ed. Springer-Verlag Berlin Heidelberg, 2000. ISBN: 978-3-662-04156-7.

[51] Amano, H., N. Sawaki, I. Akasaki, and Y. Toyoda. *Metalorganic vapor phase epitaxial growth of a high quality GaN film using an AlN buffer layer*, Applied Physics Letters **48**., 353 (1986). DOI: 10.1063/1.96549.

[52] Nakamura, S., Y. Harada, and M. Seno. *Novel metalorganic chemical vapor deposition system for GaN growth*, Applied Physics Letters **58**., 2021 (1991). DOI: 10.1063/1.105239.

[53] Amano, H., M. Kito, K. Hiramatsu, and I. Akasaki. *P-Type Conduction in Mg-Doped GaN Treated with Low-Energy Electron Beam Irradiation (LEEBI)*, Japanese Journal of Applied Physics **28**., L2112 (1989). DOI: 10.1143/jjap.28.l2112.

[54] Nakamura, S., N. Iwasa, M. Senoh, and T. Mukai. *Hole Compensation Mechanism of P-Type GaN Films*, Japanese Journal of Applied Physics **31**., 1258 (1992). DOI: 10.1143/jjap.31.1258.

[55] Staub, E. "Developing a High-Flux Atomic Beam Source for Experiments with Ultracold Strontium Quantum Gases." MA Thesis. Ludwig-Maximilians-Universität München, 2019. URL: https://ultracold.sr/publications/thesis_etienne_staub.pdf.

[56] Homeier, L. "Setup and characterization of a Littrow laser for 689 nm." BSc Thesis. Ludwig-Maximilians-Universität München, 2017. URL: https://ultracold.sr/publications/thesis_lukas_homeier.pdf.

[57] Janša, N. "A frequency-stable diode laser system for spectroscopy and trapping of Sr atoms." MA Thesis. Ludwig-Maximilians-Universität München, 2016. URL: https://www.ultracold.sr/publications/thesis_nejc_jansa.pdf.

[58] Wallner, F. MA Thesis. Technische Universität München, 2020. URL: https://ultracold.sr/publications/.

[59] Schkolnik, V., J. R. Williams, and N. Yu. *Generating 500 mW for laser cooling of strontium atoms by injection locking a high power laser diode*, arXiv: 2004.11732 (2020).

[60] Ramsey, N. *Molecular Beams*. Oxford: Oxford University Press, 1956. ISBN: 0-19-852021-2.

[61] Vanier, J. and C. Audoin. *The Quantum Physics of Atomic Frequency Standards*. Vol. 1. Bristol and Philadelphia: IOP Publishing Ltd, 1989. ISBN: 0-85274-432-3.

[62] Clausing, P. *Over den verblijftijd van moleculen en de strooming van zeer verdunde gassen*, (1928).

[63] Olander, D. R. and V. Kruger. *Molecular Beam Sources Fabricated from Multichannel Arrays. III. The Exit Density Problem*, Journal of Applied Physics **41**., 2769 (1970). DOI: 10.1063/1.1659313.

[64] Pauly, H. *Other Low-Energy Beam Sources, Atomic and Molecular Beam Methods*. Vol. 1. Oxford: Oxford University Press, 1988. ISBN: 0-19-504280-8.

[65] Yang, T., K. Pandey, M. S. Pramod, F. Leroux, C. C. Kwong, E. Hajiyev, Z. Y. Chia, B. Fang, and D. Wilkowski. *A high flux source of cold strontium atoms*, The European Physical Journal D **69**., 226 (2015). DOI: 10.1140/epjd/e2015-60288-y.

[66] Bennetts, S. "1000 times closer to a continuous atom laser: Steady-state strontium with unity phase-space density." PhD Thesis. University of Amsterdam, 2019. URL: http://www.strontiumbec.com/StrontiumLab/Theses/Shayne_Bennetts_PhD_thesis.pdf.

[67] Colzi, G., E. Fava, M. Barbiero, C. Mordini, G. Lamporesi, and G. Ferrari. *Production of large Bose-Einstein condensates in a magnetic-shield-compatible hybrid trap*, Phys. Rev. A **97**, 053625 (2018). DOI: 10.1103/PhysRevA.97.053625.

[68] Campbell, R. A. A., R. W. Eifert, and G. C. Turner. *Openstage: A Low-Cost Motorized Microscope Stage with Sub-Micron Positioning Accuracy*, PLOS ONE **9**., 1 (2014). DOI: 10.1371/journal.pone.0088977.

[69] Advanced Micro Systems LLC. *Stepper Motor Control Basics*. 2020. URL: http://stepcontrol.com/stepping101/ (visited on 12/03/2020).

[70] Douglas W. Jones. *Control of Stepping Motors. A Tutorial*. 2014. URL: https://homepage.divms.uiowa.edu/~jones/step/index.html (visited on 12/03/2020).

[71] SparkFun Electronics®. *Big Easy Driver*. URL: https://www.sparkfun.com/products/12859 (visited on 12/03/2020).

[72] Busche, H. "Efficient loading of a magneto-optical trap for experiments with dense ultracold Rydberg gases." Diploma Thesis. Department of Physics and Astronomy, University of Heidelberg, 2011. URL: https://www.physi.uni-heidelberg.de/Forschung/QD/datafiles/publications/theses/2011_Hannes_Busche.pdf.

[73] Metzger, K. *Dreidimensionale Feldberechnung starr magnetisierter Permanentmagnete mit einer Anwendung in eisenlosen elektrischen Maschinen*, Archiv für Elektrotechnik **59**., 229 (1977). DOI: 10.1007/BF01573988.

[74] Donley, E. A., T. P. Heavner, F. Levi, M. O. Tataw, and S. R. Jefferts. *Double-pass acousto-optic modulator system*, Review of Scientific Instruments **76**., 063112 (2005). DOI: 10.1063/1.1930095.

[75] Corning Inc. *Macor® Machinable Glass Ceramic*. 2012. URL: https://www.corning.com/emea/de/products/advanced-optics/product-materials/specialty-glass-and-glass-ceramics/glass-ceramics/macor.html (visited on 11/20/2020).

[76] Desai, P. D., T. K. Chu, H. M. James, and C. Y. Ho. *Electrical Resistivity of Selected Elements*, Journal of Physical and Chemical Reference Data **13**., 1069 (1984). DOI: 10.1063/1.555723.

[77] Thorlabs. *Visible Laser Diodes: Center Wavelengths from 404 nm to 690 nm*. 2020. URL: https://www.thorlabs.com/newgrouppage9.cfm?objectgroup_id=7 (visited on 12/05/2020).

[78] Sansonetti, J. E. and G. Nave. *Wavelengths, Transition Probabilities, and Energy Levels for the Spectrum of Neutral Strontium (SrI)*, Journal of Physical and Chemical Reference Data **39**., 033103 (2010). DOI: 10.1063/1.3449176.

Acknowledgements

First of all, I would like to thank my supervisor, Dr. Sebastian Blatt, for his dedication. With his help and trust, I went from not even knowing how to couple some laser light into an optical fiber to be able to work independently on my lab project. I have also appreciated the possibility to work on small main experiment related tasks from the first day. Apart from all the physics, he also taught me how to tackle problems I thought impossible by dividing them into small tasks and addressing each issue at a time. Thanks to his advice and explanations, I could really profit from the year spent in the lab.

I want to especially thank Prof. Dr. Immanuel Bloch for granting me the great opportunity of being part of his group and work in this world-class environment.

Thanks also to Dr. Neven Šantić for his advice and support. He has been of tremendous help on many occasions, where, without him, I would have been stuck for days without knowing what the problem was. He always came up with good and quick ideas to debug my setup. Good luck with the new lab!

My special thanks also go to Annie Park, for being always there for me, even on Sunday afternoons. She was always ready to help, even when super busy with the main experiment.

I also want to thank Jan Trautmann for his advice and for not getting mad at my Arduino spaghetti code. A big thank you to Valentin Klüsener and Dr. André Heinz for their help in the lab and the funny stories during lunch. Last but not least, thanks to Florian Wallner for the time shared in the prep lab discussing our projects. You have been really helpful, keeping me motivated during this whole year. It was nice to make this journey together!

Thanks also to Dimitrios Tzevas and Ylong Yang, who joined the lab at the end of my master thesis, for the interesting discussions about their projects and for trusting me by asking my advice about small stuff.

Of course, a big thank you also goes to Anton Mayer for his help with the oven and the translation stage. Without his mechanical engineering knowledge, a lot would not have been possible, and some would have taken me forever. Thanks also for not losing an occasion to make a joke while at the same time teaching me about materials and fabrication processes.

I also would like to thank all the Bloch group members for the exciting discussions and for the sense of being part of a big family that they have given me.

Finally, thanks to my family for their love and support, even when I stressed them with lab problems. Thanks also to my friends for making me feel like I had never left when I visited them back home and for pretending to understand when I bothered them with lab life issues.

Appendix A

Our Strontium Oven

A.1 Current Design

When the oven was designed, two main requirements had to be fulfilled. First of all, it had to be possible to try different capillary lengths, so the nozzle is detachable. Even now that we know which capillaries we want to use, it still makes sense to keep it like this to allow a more comfortable substitution if something breaks. Second, the oven has to run at temperatures up to 900 °C with a large temperature gradient between the nozzle and the crucible to avoid clogging of the nozzle. Additional requirements were easy reloading, compatibility with the main experiment setup, low power consumption, and minimal heating of the surrounding. Some of these requirements have been met; some still need improvement. We will now have a brief look at the different parts that constitute the oven, focusing on those that need a redesign. For all the construction details, the materials choice, and the test setups, see Ref. [55].

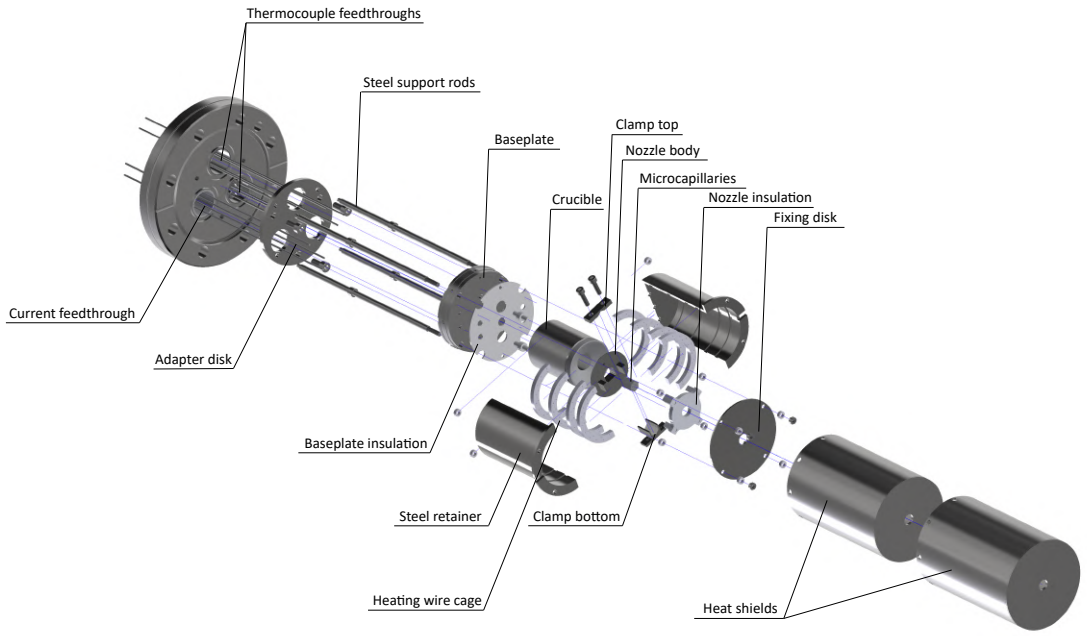

Figure A.1 Exploded view of the oven.

The oven has been constructed with a "bottom-up" approach to enable easy loading, as displayed in Fig. A.1. This way, when loading new strontium, we have to remove just the uppermost layers. Let us have a look at the most significant components of the oven.

Dimensions and Materials

The dimensions were set taking two aspects into account: the capability to load 25 g of distilled dendritic strontium (the standard amount contained in a large ampule from Sigma-Aldrich Chemie GmbH: 460346-5G) and the compatibility with the main experiment setup. For this reason, the whole setup was mounted on a CF63 flange. The length was kept 154 mm to keep the setup compact.

We used stainless steel EN 1.4841, which is suitable for the purpose due to its mechanical strength at high temperatures and its low magnetic susceptibility. The only exceptions are the capillaries, manufactured from EN 1.4301. This was due to a shortage of commercially available 1.4841 tubing. There are actually other materials that could be used, for example, Monel 400 or Inconel 600, but this would have been much more expensive. The parts supporting the heating wire or with an insulating function have been made out of Macor, a type of glass ceramic developed by Corning Inc. [75]. Last but not least, the heating wire was chosen to be made of tantalum, which has a melting point of 3017 °C and an electrical resistivity $\rho \sim 50 \times 10^{-8}\ \Omega$m, two times the one of tungsten, another commonly used material [76].

Crucible and Nozzle

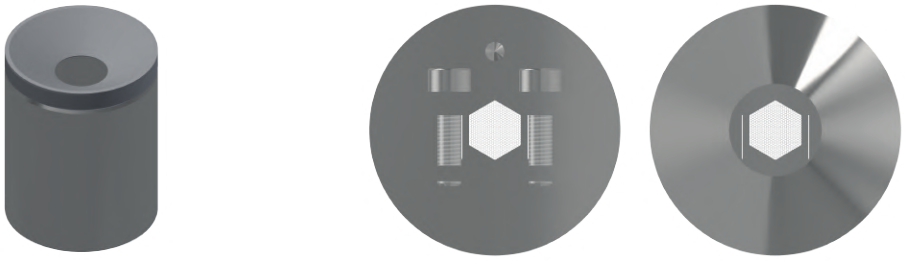

(a) **(b)**

Figure A.2 (a) Crucible render. The top part is conical with an angle of 120° to prevent fusing to the nozzle and to block strontium from creeping to the nozzle. (b) Front and back view of the nozzle.

Inside the crucible, strontium gets heated up to 750°C. After sublimating, it effuses through the nozzle capillaries. The crucible has a conical design for several reasons. First, to avoid clogging of the nozzle caused by strontium creeping towards the nozzle. Second, to inhibit fusing to the nozzle and third to guide strontium pieces into the crucible if they have been badly loaded. The angle of 120° will also be maintained in the

next iteration, which will contribute to set the size of the system.

The nozzle has a detachable design that does not require screws to hold it in place. The nozzle's position is fixed with a Macor insulating plate and a fixing disk, as shown in Figure A.1. The capillaries are clamped inside a hexagonal insert since this shape provides the highest packing density. The microcapillaries were manufactured by Robert-Helwig GmbH to be burr-free cut to avoid artificial broadening of the atomic beam.

Heating Circuits and Heat Shields

To avoid having to use electrically insulating materials, the heating was designed to be radiative. The second requirement is a large temperature gradient between the nozzle and crucible. A small gradient has shown to be the main cause of clogging. To achieve a large gradient, two separate circuits were used, one running just around the nozzle and one along the whole length. To avoid contact with the steel parts, the wires go through holes drilled in Macor half-moon pieces. The wire's length was limited by the lab power supplies, the density by the allowed bending radius. The Macor disks are held in place by steel retainers in the form of half-cylinders. The current for the wires is supplied by two lab supplies (EA Elektro-Automatik: EA-PS 3065-05 B) connected to 4 current feedthroughs (VACOM: W-HV3-4CE-NI13). The temperature is monitored via K-type thermocouples s (Omega: OV-1-20-K-12) connected to thermocouple feedthroughs (VACOM: W-TC2-CE-K).

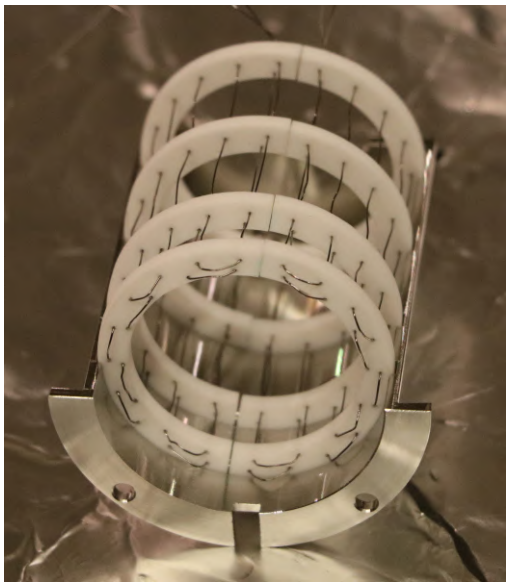

Figure A.3 Heating circuits threaded through the Macor pieces.

Running the oven, we noticed that just the nozzle circuit was enough to heat everything

up. This means that we have currently no control over the gradient. Fig. A.4 shows a graph of the temperature increase.

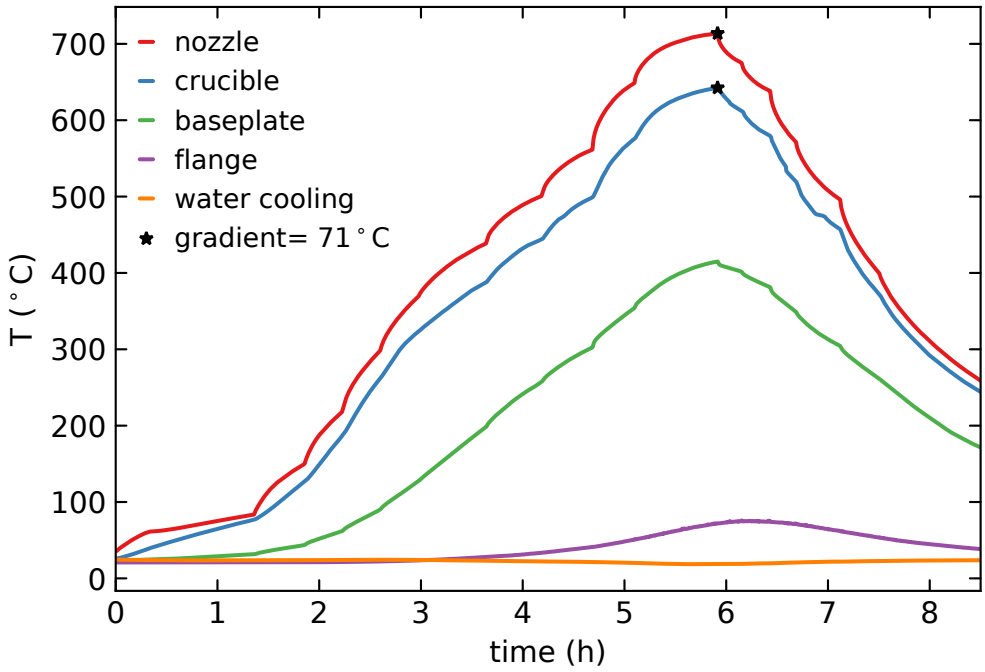

Figure A.4 Temperatures recorded at the nozzle, crucible, base plate, and outside the oven. The maximum temperature difference obtained is marked with an asterisk.

We would like to decouple the two elements and be able to run them independently. It is not possible to physically decouple the circuits more than they are now. This would not even improve the situation since the nozzle and crucible are already coupled, independently of the heating circuits. The only way to solve this is to cool the crucible through a better thermal contact between its bottom and the oven baseplate.

Other essential elements to produce a large temperature gradient are the two heat shields stacked around the steel retainers. When designed, the aim was to reduce power consumption, reflecting the heat back to the nozzle and the crucible. Simultaneously, they should prevent the heat from transferring to the outer part of the oven. While testing the oven, it was noticed that if they were just cylinders without a top plate, the gradient achieved was low, and the capillaries got clogged. On the other hand, the presence of a top plate with a hole in it, helped to reflect the heat back to the nozzle and resulted in an unclogged nozzle. We are still not satisfied, as mentioned in chapter 4, strontium might be effusing from these shields or from some other element of the oven that gets too hot. From there, the atoms would effuse with a cosine distribution. This will broaden the

beam and nullify all the work done by the capillaries. This is probably what is happening to our beam. This hypothesis is strengthened by what is shown in Fig. A.4: the flange gets really hot, which makes us believe that the shields become also really hot. The flange reaches around 90°C even with just an afternoon of operation at high temperature. The plan was to use this oven in the main experiment, but we will run the oven for even longer, and we cannot have such high temperatures that will affect all the optics and sensitive elements in the setup. Moreover, it will cause outgassing and increase the vacuum pressure. We need a way of cooling the flange. Right now, copper tubing is wound around the front part of the oven, but this is obviously not enough. The plan is to implement in-vacuum water cooling. The idea is to use tubing surrounding the steel retainer connected to a plate lying in front of the nozzle. The plate should have holes to reduce pressure and to allow atoms to pass through it. At the same time the presence of in-vacuum water cooling will keep this plate colder, so atoms should not effuse from there.
We also plan to increase the nozzle diameter, with an inner circle diameter of 10 mm and about 1261 microcapillaries. We plan to keep the aspect ratio $\beta = 0.02$ since this has shown to be a good compromise to avoid clogging while still having a good collimating action. This increased size and the additional cooling elements will require a CF100 flange.

Appendix B

Zeeman Slower Repumping

We mentioned in chapter 2, that we would like to use a repump scheme also for the Zeeman slower. To do that we need to address the 448 nm transition shown in Fig. 2.1. For these reason we tested different Thorlabs diodes to find out if they had a spectrum compatible with what we needed. The diodes are the L450P1600MM and the L450G1. As shown in Table B.1, the center wavelength is different from what we need, but the spectra are broad so we might still be able to obtain what we want by tuning the temperature. The main advantage would of course be the high power generated by these diodes: 1.6 and 3 W.

LD	Wavelength	Power	Typical drive current	Spatial mode
L450P1600MM	450 nm	1600 mW	1200 mA	multimode
L450G1	447 nm	3000 mW	2000 mA	multimode

Table B.1 Laser diode specifications from Ref. [77].

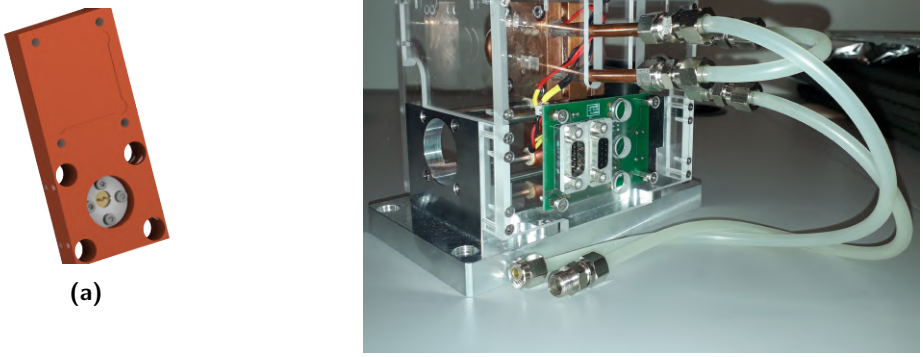

(a) **(b)**

Figure B.1 (a) L450G1 copper mount. (b) Assembled laser.

We mounted both the diodes inside an acrylic housing originally designed for tapered amplifiers. The diode is placed inside a copper element and fixed with four screws, to enhance the thermal contact we placed a indium foil between the fixing disk and the

diode case. The copper element has a hole in it to house a thermistor, this has been glued there with EPO-TEK® H74. On the sides of the copper element there are two "slots" to place the Peltier elements. These are then fixed in place thanks to two other copper elements. The thermal contact is increased using heat paste. Water can flow through these two elements. The whole structure rests then on metal rods, followed by a collimating lens.

The protection board is basically the same as in Fig. 3.5, but we are now using Thorlabs controllers ITC4001/ITC4005, which requires cutting of pin 8 for the temperature controller and $0\ \Omega$ resistors in place of the $22\ \Omega$ ones.

B.1 Laser Characterization

Before trying out the lasers with atomic beams, we checked the output power and the spectra.

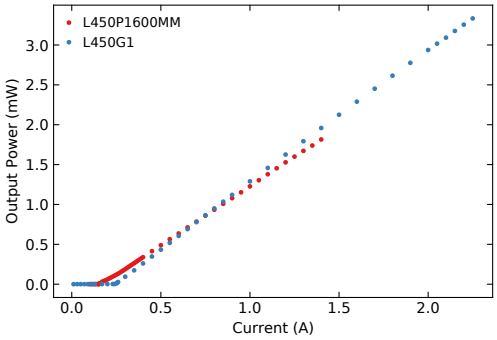

Figure B.2 Output power of the two lasers.

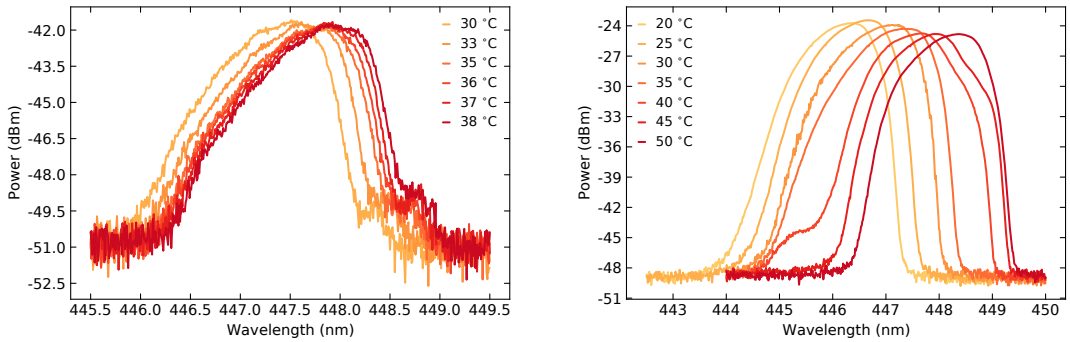

(a) **(b)**

Figure B.3 (a) L450G1 for $I = 2.5$ A. (b) L450P1600MM for $I = 1.49$ A.

As we can see from Fig. B.3, both lasers require high temperature to get to the wavelength that we need. The 1.6 W diode was too sensitive to temperature and was not stable, so we resort to the 3 W laser. Another thing to keep in mind is the presence of the 444 nm transition from 5s5p $^3P_2$ to 5s7s $^3S_1$, which we do dot want to excite [78]. For this reason we use a filter to clean the spectrum (Semrock LL01-458-25).

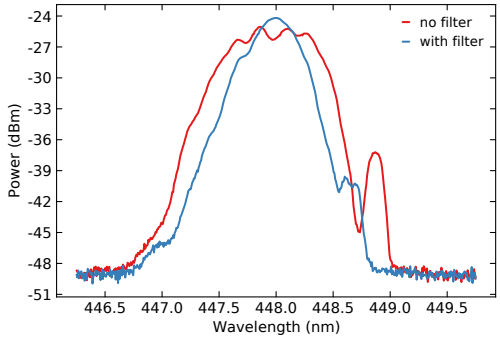

Figure B.4 Example of the effect of the filter on the laser spectrum.

Due to time constraints it was not possible to really demonstrate the effect of the repump beam. Preliminary tests have shown a promising increase of the number of atoms loaded in our MOT, but the setup still requires investigation, especially to find out if the setup is stable. For completeness we will now briefly describe how we would measure the atom number increment.

B.2 Atom Number Measurement

In the main experiment the atomic beam is collimated in the transverse cooling region and slowed down by the Zeeman slower. Atoms reach then the main chamber where we capture them with a MOT without repumping. This means that the atoms decay to $^3P_2$, which can be trapped in the MOT field. After loading in the magnetic trap we turn off blue light and apply repump lasers to go back to the ground state. From that point starts the red MOT stage. If we pump while maintaining the blue MOT, the atoms back in $^1S_0$ get trapped in the MOT, there they scatter light, so the fluorescence increases. We measure it with an avalanche photodiode mounted on the top of the chamber. The sequence for atom number measurement is the following: we first get rid of atoms from previous cycles by shining repump light, so that they decay to the untrapped ground state. We then shine blue MOT light to check if we actually removed the atoms. The measurement starts with magnetic trap loading, when doing the atom number measurement the loading is stopped after 1 s. The atoms are held for enough time to be sure that the shutter is really closed. Finally we shine repump and MOT light and detect the fluorescence.

Eidesstattliche Erklärung

Erklärung:
Hiermit erkläre ich, die vorliegende Arbeit selbständig verfasst zu haben und keine anderen als die in der Arbeit angegebenen Quellen und Hilfsmittel benutzt zu haben.

München, Datum der Abgabe

Unterschrift